nature ecology & evolution

ARTICLES

https://doi.org/10.1038/s41559-020-01327-6

OPEN

Conservative route to genome compaction in a miniature annelid

José M. Martín-Durán[1,2] ✉, Bruno C. Vellutini[1,3,16], Ferdinand Marlétaz[4,13,16], Viviana Cetrangolo[1,5], Nevena Cvetesic[6], Daniel Thiel[1,14], Simon Henriet[1], Xavier Grau-Bové[7], Allan M. Carrillo-Baltodano[2], Wenjia Gu[2], Alexandra Kerbl[8,15], Yamile Marquez[9], Nicolas Bekkouche[8], Daniel Chourrout[1], Jose Luis Gómez-Skarmeta[10], Manuel Irimia[9,11,12], Boris Lenhard[1,6], Katrine Worsaae[8,17] and Andreas Hejnol[1,5,17] ✉

The causes and consequences of genome reduction in animals are unclear because our understanding of this process mostly relies on lineages with often exceptionally high rates of evolution. Here, we decode the compact 73.8-megabase genome of *Dimorphilus gyrociliatus*, a meiobenthic segmented worm. The *D. gyrociliatus* genome retains traits classically associated with larger and slower-evolving genomes, such as an ordered, intact Hox cluster, a generally conserved developmental toolkit and traces of ancestral bilaterian linkage. Unlike some other animals with small genomes, the analysis of the *D. gyrociliatus* epigenome revealed canonical features of genome regulation, excluding the presence of operons and *trans*-splicing. Instead, the gene-dense *D. gyrociliatus* genome presents a divergent Myc pathway, a key physiological regulator of growth, proliferation and genome stability in animals. Altogether, our results uncover a conservative route to genome compaction in annelids, reminiscent of that observed in the vertebrate *Takifugu rubripes*.

Animals, and eukaryotes generally, exhibit a striking range of genome sizes across species[1], seemingly uncorrelated with morphological complexity and gene content. This has been deemed the 'C-value enigma'[2]. Animal genomes often increase in size due to the expansion of transposable elements (TE) (for example, in rotifers[3], chordates[4,5] and insects[6]) and through chromosome rearrangements and polyploidization (for example, in vertebrates[7–9] and insects[10]), which is usually counterbalanced through TE removal[11], DNA deletions[12,13] and rediploidization[14]. Although the adaptive impact of these changes is complex and probably often influenced by neutral non-adaptive population dynamics[15,16], genome expansions might also provide new genetic material that can stimulate species radiation[7] and the evolution of new genome regulatory contexts[17] and gene architectures[18]. By contrast, the evolutionary drivers of genome compaction are more debated and hypotheses are often based on correlative associations[1]; for example, with changes in metabolic[19] and developmental rates[20], cell and body sizes[1,21] (as in some arthropods[22,23], flatworms[22] and molluscs[24]) and the evolution of radically new lifestyles, such as powered flight in birds and bats[13,25] and parasitism in some nematodes[26,27] and orthonectids[28]. However, these correlations often suffer from multiple exceptions; for example, not all parasites have small genomes[27] neither does the insect with arguably the smallest body size have a compact genome[29] and thus they probably reflect lineage-specific specializations instead of general trends in animal evolution. In addition, genomic compaction leading to minimal genome sizes, as in some free-living species of nematodes[30], tardigrades[31,32] and appendicularians[5,33], apparently co-occurs with prominent changes in gene repertoire[34,35], genome architecture (for example, loss of macrosynteny[36]) and genome regulation (for example, *trans*-splicing and operons[37–39]), yet these divergent features are also present in closely related species with larger genomes[5,32,40]. Therefore, it is unclear whether these are genomic changes required for genomic streamlining or lineage specializations unrelated to genome compaction.

The marine annelid *Dimorphilus gyrociliatus* (O. Schmidt, 1857) (formerly *Dinophilus gyrociliatus*) has been reported to have a C-value (haploid genome size) of only 0.06–0.07 pg (~59–68 megabases, Mb)[41], the smallest ever reported for an annelid[42], and a haploid karyotype of 12 chromosomes[43]. *D. gyrociliatus* is a free-living meiobenthic species[44] whose adults show strong sexual dimorphism, evident already during embryogenesis (Fig. 1a). The adult females are ~1 mm long and display a typical, albeit simplified, annelid segmental body plan[45] with only six segments, reduced coelom, and no appendages, parapodia or chaetae (Supplementary Note 1). *D. gyrociliatus* males are, however, only 50 µm long, comprise just a few hundred cells, lack a digestive system but still possess highly

[1]Sars International Centre for Marine Molecular Biology, University of Bergen, Bergen, Norway. [2]School of Biological and Chemical Sciences, Queen Mary University of London, London, UK. [3]Max Planck Institute of Molecular Cell Biology and Genetics, Dresden, Germany. [4]Molecular Genetics Unit, Okinawa Institute of Science and Technology, Graduate University, Onna, Japan. [5]Department of Biological Sciences, University of Bergen, Bergen, Norway. [6]Institute for Clinical Sciences and MRC London Institute of Medical Sciences, Faculty of Medicine, Imperial College London, London, UK. [7]Department of Vector Biology, Liverpool School of Tropical Medicine, Liverpool, UK. [8]Department of Biology, University of Copenhagen, Copenhagen, Denmark. [9]Centre for Genomic Regulation, Barcelona Institute of Science and Technology, Barcelona, Spain. [10]Centro Andaluz de Biología del Desarrollo, Consejo Superior de Investigaciones Cientificas-Universidad Pablo de Olavide-Junta de Andalucía, Seville, Spain. [11]Universitat Pompeu Fabra, Barcelona, Spain. [12]ICREA, Barcelona, Spain. [13]Present address: Centre for Life's Origins and Evolution, Department of Genetics, Evolution and Environment, University College London, London, UK. [14]Present address: Living Systems Institute, University of Exeter, Exeter, UK. [15]Present address: Centrum für Naturkunde, Universität Hamburg, Hamburg, Germany. [16]These authors contributed equally: Bruno C. Vellutini, Ferdinand Marlétaz. [17]These authors jointly supervised this work: Katrine Worsaae, Andreas Hejnol. ✉e-mail: chema.martin@qmul.ac.uk; andreas.hejnol@uib.no

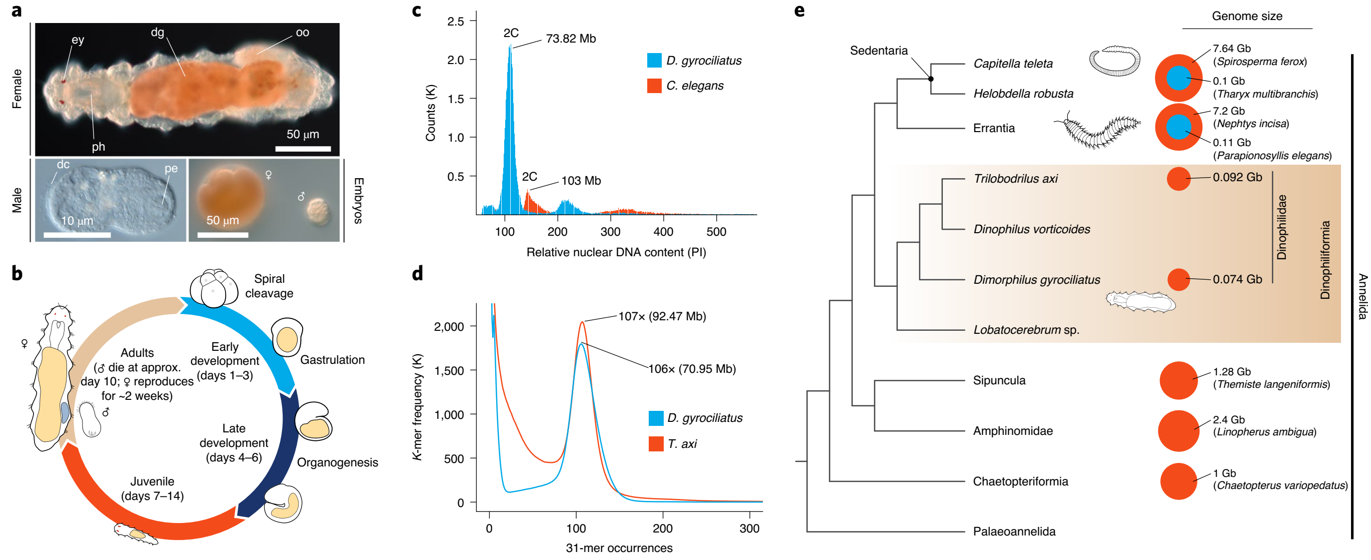

Fig. 1 | *D. gyrociliatus* has the smallest annelid genome. a, Differential interference contrast images of adults and embryos of *D. gyrociliatus*. The adults are miniature annelid worms with an extreme sexual dimorphism, already apparent during early embryogenesis. **b**, The life cycle of *D. gyrociliatus* comprises a 6-day-long embryogenesis with a canonical early spiral cleavage programme, followed by a juvenile and an adult, reproductively active stage. **c**, Flow cytometry analysis using the nematode *C. elegans* as reference and propidium iodide (PI) nuclear intensity estimates the genome size of *D. gyrociliatus* as 73.82 Mb. **d**, *K*-mer counts estimate the genome size of *D. gyrociliatus* and *T. axi* to be 70.95 Mb and 92.47 Mb, respectively. **e**, *D. gyrociliatus* and *T. axi* belong to Dinophiliformia, the sister group to Sedentaria and Errantia, and their genome sizes are the smallest known among annelids. dc, dorsal ciliary field; dg, digestive system; ey, eye; oo, oocyte; pe, penis; ph, pharynx. Drawings are not to scale.

specialized sensing and copulatory organs[46]. Despite their miniature size, *D. gyrociliatus* retain ancestral annelid traits, such as a molecularly regionalized nervous system in the female[47,48] and the typical quartet spiral cleavage[49] (Fig. 1b). With only a few genomes sequenced (Supplementary Table 1), annelids have retained ancestral spiralian and bilaterian genomic features[50]. Therefore, *D. gyrociliatus*, with its reduced genome size and small body, is a unique system in which to investigate the genome architecture and regulatory changes associated with genome compaction and to assess the interplay between genomic and morphological miniaturization.

Results

We performed long-read PacBio sequencing (Extended Data Fig. 1a) to generate a highly contiguous (N50, 2.24 Mb) and complete (95.8% BUSCO genes) ~78 Mb-long haploid assembly, comparable in quality to other published annelid genomes (Extended Data Fig. 1d,e and Supplementary Table 1). Flow cytometry measurements and *K*-mer based analyses estimated the size of *D. gyrociliatus* genome to be 73.82 Mb and 70.95 Mb, respectively (Fig. 1c,d), agreeing with previous estimations[41]. While their simple morphology originally prompted them to be considered as early-branching annelids[51] ('Archiannelida'), molecular phylogenies later placed *D. gyrociliatus* either within Sedentaria[52] or as sister to Errantia and Sedentaria[53], the two major annelid clades (Supplementary Note 2). Gathering an extensive dataset of annelid sequences[54], we robustly placed *D. gyrociliatus* together with *Trilobodrilus axi*, *Dinophilus vorticoides* and *Lobatocerebrum* sp.—all miniature annelids—in a clade we name Dinophiliformia that is sister to Errantia and Sedentaria, thus confirming the previous proposal[53] (Fig. 1e and Extended Data Fig. 2). Given the generally larger bodies and genome sizes found in annelid lineages outside Dinophiliformia (Fig. 1e), and that *T. axi* also has a compact, 92.47 Mb genome (Fig. 1d), our data suggest genome size reduction and morphological miniaturization both occurred in the lineage leading to *D. gyrociliatus* and its relatives.

To assess how changes in repeat content contributed to genome reduction in *D. gyrociliatus*, we annotated the complement of TEs, uncovering a much lower percentage (4.87%) than in other annelid genomes (Fig. 2a and Extended Data Fig. 3a,b). Most TEs (91.5%) group in four classes and, as in the annelid *Helobdella*[50], TEs are either old copies or very recent expansions (Fig. 2b). The most abundant TE class is a Ty3-*gypsy*-like long terminal repeat (LTR) retrotransposon that appears to be an annelid- or *D. gyrociliatus*-specific subfamily, and thus we name it Dingle (Dinophilidae *Gypsy*-like elements) (Extended Data Fig. 3c). As in some insect and nematode clades[55], where LTR retrotransposon *envelope* (*env*) proteins are apparently related to *env* proteins of DNA viruses, Dingle *envelope* (*env*) protein shows similarities with envelope glycoprotein B precursors of cytomegalovirus (CMV) and herpesviridae-1 (HSV-1) (Extended Data Fig. 3d,e). Compared to species with minimal genome sizes, *D. gyrociliatus* TE load is three to four times lower than in the appendicularian *Oikopleura dioica* and the tardigrade *Ramazzottius varieornatus* but around four times larger than in insects with larger, still compact genomes (~100 Mb) (Supplementary Table 5). Therefore, TE depletion contributed to genome compaction in *D. gyrociliatus* but this does not appear to be the main driving factor since other small animal genomes show even lower fractions of TEs.

To explore how changes in gene architecture influenced genome compaction, we used transcriptomic data and ab initio predictions to annotate 14,203 protein-coding genes in the *D. gyrociliatus* genome, a smaller gene repertoire than that of other annelids (Fig. 2c, Extended Data Fig. 1b,c and Supplementary Table 1). However, the gene number is comparable to free-living species with similar genome sizes, such as *O. dioica*[33] (~15,000 genes) and *R. varieornatus*[32] (~14,000 genes). With a gene density (208.86 genes per Mb) double that in the annelids *Capitella teleta* (99.96 genes per Mb) and *Helobdella robusta* (97.5 genes per Mb), *D. gyrociliatus* has shorter intergenic regions and transcripts, but similar exon lengths and even larger untranslated regions (UTRs) (Extended Data Fig. 4a,b,d–f), suggesting that intron shortening might have contributed to genome compaction. However, although *D. gyrociliatus* shows overall very short introns (median 66 base pairs, bp)

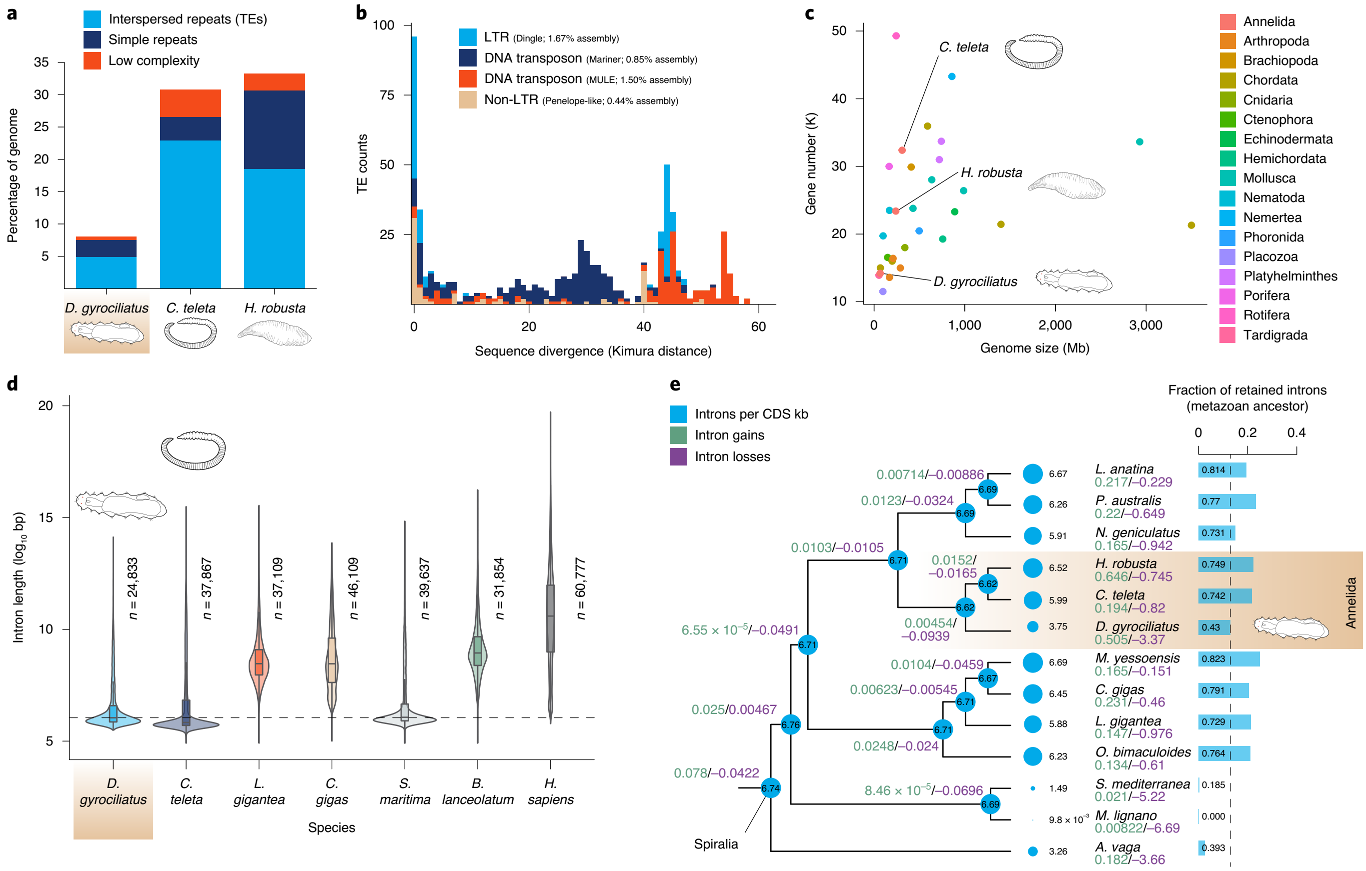

Fig. 2 | *D. gyrociliatus* has a reduced transposable element and intronic landscape. a, The percentage of the genome assigned to TEs and repeats in three annelid genomes. *D. gyrociliatus* has considerably less TEs and simple repeats than other annelids. **b**, TE abundance according to sequence divergence (Kimura distance) to family consensus. TE expansions are limited in size and correspond to either very recent bursts or old elements. **c**, Number of annotated genes in 28 animal genomes plotted against genome size. *D. gyrociliatus* has a reduced gene repertoire compared to other annelids but comparable to other animals of similar genome size. **d**, Size distribution of orthologous introns in seven bilaterian species. Intron size is comparable between *D. gyrociliatus* and the annelid *C. teleta* and the centipede *S. maritima*, which are both slow-evolving lineages with larger genomes. Dashed horizontal line indicates *D. gyrociliatus* median intron size. **e**, Rates of intron gain (green), intron loss (violet) and introns per kb of CDS (blue) in representative spiralian lineages and a consensus phylogeny. *D. gyrociliatus* has lost introns, yet at a much lower rate and preserving many more ancestral animal introns than other fast-evolving spiralian lineages, such as flatworms and rotifers. Note that intron densities in the platyhelminthes *S. mediterranea* and *M. lignano* are underestimated due to the low fraction of single-copy complete orthologues detected in these species for the BUSCO gene dataset.

and its splicing is thus more efficient at removing short intron sizes (Extended Data Fig. 4i), introns are not shorter on average than in *C. teleta* (median 57 bp) and even similar to the centipede *Strigamia maritima* (median 67 bp) (Fig. 2d and Extended Data Fig. 4h), both with larger genomes than *D. gyrociliatus*. Instead, *D. gyrociliatus* has fewer introns than other annelids (Fig. 2e) and exhibits an intron density comparable to other animals with small genome sizes, such as *O. dioica* and *C. elegans*, but with a much higher retention of ancestral introns (Extended Data Fig. 4j,k). Therefore, gene and intron loss, rather than short intron size—which was probably a pre-existing condition—correlates with genome compaction in *D. gyrociliatus*, unlike in free-living nematodes of similar genome size[56].

To investigate how gene loss shaped the *D. gyrociliatus* genome and morphology, we first reconstructed clusters of orthologous genes using a dataset of 28 non-redundant proteomes covering major animal groups and estimated gene loss and gain rates. Over 80% of *D. gyrociliatus* genes are assigned to multispecies gene families; the highest percentage in any annelid sequenced so far (Extended Data Fig. 5a). However, 38.9% of the genes in *D. gyrociliatus* are in orthogroups where there is only one *D. gyrociliatus* sequence, and thus *D. gyrociliatus* has the smallest average gene family size among annelids (1.63 genes per orthogroup; Supplementary Table 7). Although the rate of gene family loss is greater than in *C. teleta*, an annelid species with a conservatively evolving genome[50], gene loss in *D. gyrociliatus* is similar to those of the annelids *H. robusta* and *Hydroides elegans*, species with larger genomes (Fig. 3a and Extended Data Fig. 5b). Therefore, our data suggest that reduction of gene family size outweighs complete gene family loss, and thus probably underpins the reduced total gene number of *D. gyrociliatus*, as also observed in certain *Caenorhabditis* species of small genome size[56,57]

Consistent with the streamlining of its gene repertoire, we detected only nine expanded gene families in *D. gyrociliatus* (but 73 and 42 in *C. teleta* and *H. robusta*, respectively), most of them corresponding to locally duplicated genes implicated in immune responses (Extended Data Fig. 5c–e). In addition, *D. gyrociliatus* shows canonical repertoires of gene families expanded in other annelids, such as G-protein-coupled receptors (GPCRs) and epithelial sodium channels (ENaCs)[50] (Extended Data Fig. 6a,b and Supplementary Table 8). The GPCR complement of genomes is dynamic and often linked to specific (neuro)physiological adaptations, as seen in lineages with miniature genomes that have experienced either losses (for example, *O. dioica* lacks Class C, glutamate

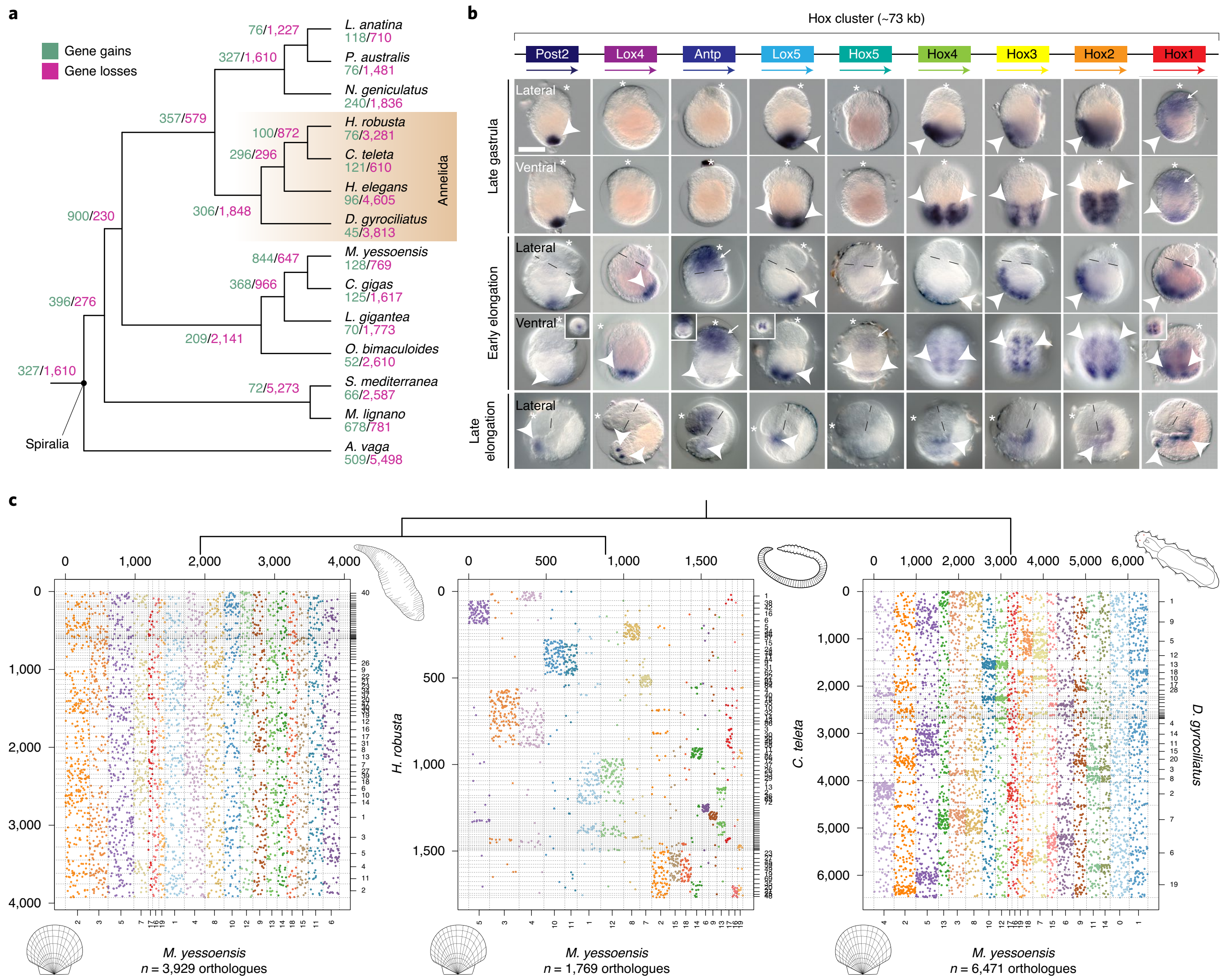

Fig. 3 | *D. gyrociliatus* has retained a conserved developmental toolkit and ancestral linkage blocks. a, Number of gene family gains (green) and losses (violet) in representative spiralian lineages under a consensus tree topology. Gene loss in *D. gyrociliatus* is similar to or lower than that observed in other fast-evolving spiralian lineages. **b**, *D. gyrociliatus* has a conserved Hox complement, organized in a compact cluster (top). Whole-mount in situ hybridization during embryogenesis reveals that Hox genes exhibit staggered anteroposterior domains of expression, but not temporal collinear expression domains (arrowheads) along the trunk region, with *Hox1*, *Hox5* and *Antp* further exhibiting anterior head expression domains (arrows). Dashed lines in lateral views of early and late elongation timepoints demarcate the head–trunk boundary and asterisks mark the anterior end. Scale bar, 50 µm. **c**, Oxford dot plots of orthologous genes between the scallop *M. yessoensis* and three annelid genomes. Orthologous genes are coloured according to their position in *M. yessoensis* linkage groups. The presence of an organized Hox cluster correlates with the preservation of some macrosyntenic blocks (areas of higher density of shared orthologues) in *D. gyrociliatus*, which are lost in the fast-evolving *H. robusta*.

receptors) or expansions (for example, *C. elegans*[58] and *R. varieornatus*[59] expanded Class A, rhodopsin receptors) (Extended Data Fig. 6b). Thus, the conserved GPCR repertoire and the canonical neuropeptide complement (Extended Data Fig. 6c) further support that *D. gyrociliatus* nervous system is functionally equivalent to, although morphologically smaller than, that of larger annelids[47,48].

Despite its miniature body plan, *D. gyrociliatus* has an overall conserved developmental toolkit at the level of both transcription factors and signalling pathways (Extended Data Fig. 5f,g). *D. gyrociliatus*, and Dinophilidae generally, exhibit a limited repertoire of certain extracellular signalling molecules (for example, Wnt and TGF-β ligands) and lacks bona fide FGF and VEGF ligands (Extended Data Fig. 5g–i). However, these simplifications do not affect the receptor repertoire (Extended Data Fig. 5j). Unlike appendicularians[60], tardigrades[32] and nematodes[32] with compact genomes, *D. gyrociliatus* exhibits a compact, ordered Hox cluster, only lacking *lox2* and *post1* (Fig. 3b and Extended Data Fig. 7a,b). In other annelids[61,62], *post1* is separate from the main Hox cluster, and as in brachiopods[63], it is expressed in chaetoblasts[62], supporting the homology of this new cell-type[63]. Remarkably, the distantly related *H. robusta* and *D. gyrociliatus* both lack chaetae, *post1* and FGF ligand (also expressed in annelid chaetoblasts; Extended Data Fig. 5k–r), suggesting that the secondary loss of chaetae followed convergent routes of gene loss in different annelid species.

To investigate whether the clustered Hox genes of *D. gyrociliatus* exhibit temporal collinearity, we first performed comparative transcriptomics at four different stages of the *D. gyrociliatus* female life cycle (Extended Data Fig. 8a,b). Genome-wide expression dynamics revealed five main clusters of coregulated genes (Extended Data Fig. 8c), corresponding to major developmental events, such as cell

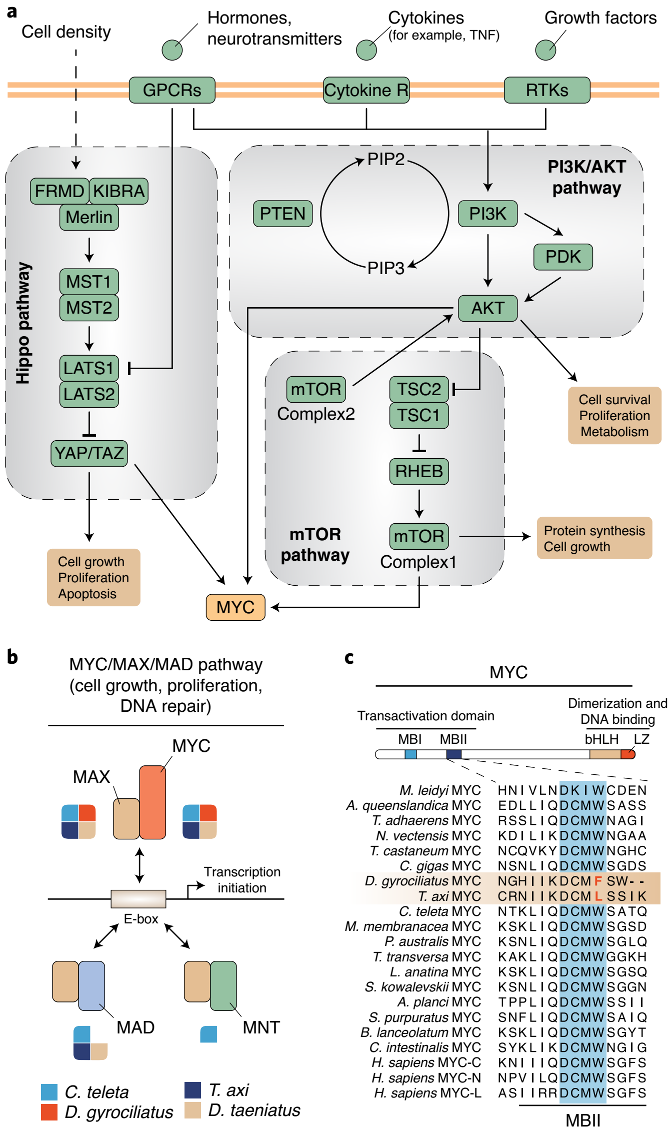
a
Cell density
Hormones, neurotransmitters
Cytokines (for example, TNF)
Growth factors
GPCRs
Cytokine R
RTKs
Hippo pathway
FRMD
KIBRA
Merlin
MST1
MST2
LATS1
LATS2
YAP/TAZ
PIP2
PIP3
PTEN
PI3K
PDK
AKT
PI3K/AKT pathway
mTOR Complex2
TSC2
TSC1
RHEB
mTOR Complex1
mTOR pathway
Cell survival Proliferation Metabolism
Protein synthesis Cell growth
Cell growth Proliferation Apoptosis
MYC
b
MYC/MAX/MAD pathway (cell growth, proliferation, DNA repair)
MYC
MAX
Transcription initiation
E-box
MAD
MNT
C. teleta
D. gyrociliatus
T. axi
D. taeniatus
c
MYC
Transactivation domain
Dimerization and DNA binding
MBI
MBII
bHLH
LZ
M. leidyi MYC HNIVLNDKIWCDEN
A. queenslandica MYC EDLLIQDCMWSASS
T. adhaerens MYC RSSLIQDCMWNAGI
N. vectensis MYC KDILIKDCMWNGAA
T. castaneum MYC NCQVKYDCMWNGHC
C. gigas MYC NSNLIQDCMWSGDS
D. gyrociliatus MYC NGHIIKDCMFSW--
T. axi MYC CRNIIKDCMLSSIK
C. teleta MYC NTKLIQDCMWSATQ
M. membranacea MYC KSKLIQDCMWSGSD
P. australis MYC KSNLIQDCMWSGLQ
T. transversa MYC KAKLIQDCMWGGKH
L. anatina MYC KSKLIQDCMWSGSQ
S. kowalevskii MYC KSNLIQDCMWSGGN
A. planci MYC TPPLIQDCMWSSII
S. purpuratus MYC SNFLIQDCMWSAIQ
B. lanceolatum MYC KSKLIQDCMWSGYT
C. intestinalis MYC SYKLIKDCMWNGIG
H. sapiens MYC-C KNIIIQDCMWSGFS
H. sapiens MYC-N NPVILQDCMWSGFS
H. sapiens MYC-L ASIIRRDCMWSGFS
MBII

Fig. 4 | *D. gyrociliatus* exhibits a divergent MYC pathway. a, Schematic representation of signalling pathways involved in cell growth/proliferation and organ size in animals. *D. gyrociliatus* shows conserved Hippo and PI3K/Akt/mTOR pathways (green boxes), but also divergences in the MYC pathway (orange box), one of the downstream regulators. See main text and Supplementary Table 11 for a complete list of genes. **b**, Schematic representation of the MYC/MAX/MAD pathway and the interactions between the main protein partners. *D. gyrociliatus* lacks bona fide MAD and MNT proteins (the latter also absent in other members of Dinophilidae). **c**, Multiple protein alignment of the MBII repressor domain of MYC, highlighting how Dinophilidae exhibit point mutations in the critical tryptophan (W) residue.

proliferation in early development or during adult growth (clusters 5 and 4, respectively), sex differentiation (cluster 2), nervous system maturation during late embryogenesis and postembryogenesis (cluster 1) and increased metabolism after hatching (cluster 3). While there is a gradual increase in gene upregulation as embryogenesis proceeds, which stabilizes in the juvenile to adult transition (Extended Data Fig. 8d–f), all Hox genes but *Hox5*, *Antp* and *post2* are expressed during early embryogenesis (days 1–3; Extended Data Fig. 7c). Using whole-mount in situ hybridization, we identified late gastrula (~3 d after egg deposition) as the earliest stage at which most Hox genes become simultaneously transcribed, including *post2* (Fig. 3b), altogether suggesting that *D. gyrociliatus* Hox genes lack temporal collinearity. Different from other annelid species[64–66], *D. gyrociliatus* embryogenesis is slow, taking ~6 d from egg laying to hatching (Fig. 1b), and thus it is unlikely that Hox temporal collinearity is compressed to span a short and quick early morphogenesis. During body elongation and segment formation, Hox genes are expressed in staggered anteroposterior domains along the developing trunk, in patterns resembling those of *C. teleta*[62], further supporting that *D. gyrociliatus* retains the ancestral annelid molecular body patterning (Fig. 3b and Extended Data Fig. 7d). Therefore, *D. gyrociliatus* Hox genes show only staggered expression domains along the anteroposterior axis (Extended Data Fig. 7e), providing a compelling case where temporal collinearity is not driving Hox cluster compaction and maintenance[67].

Animal groups with reduced genome sizes show altered gene orders, as exemplified by their disorganized Hox clusters[60,68] and the loss of conserved gene linkage blocks that represent the ancestral chromosomal organization[36,50]. In *O. dioica*, this loss has been related to the loss of the classical non-homologous end-joining, double-strand DNA break repair pathway[69]. In addition to an ordered Hox cluster, *D. gyrociliatus* shows residual conservation of ancestral linkage blocks, which appear eroded but still visible (Fig. 3c). These blocks are almost intact in *C. teleta* but completely lost in *H. robusta* (Fig. 3c and Extended Data Fig. 7f). Moreover, *D. gyrociliatus* has a conserved double-strand DNA break repertoire (Supplementary Table 9), with the exception of BRCA1, which is however also absent in other invertebrates capable of homologous recombination, such as *Drosophila melanogaster*[70]. Therefore, mutation-prone double-strand DNA break repair mechanisms that can increase DNA loss do not underpin genomic compaction in *D. gyrociliatus*, which occurred without drastic genome architecture rearrangements.

Changes in genome size have been positively correlated to differences in cell and body sizes in a range of animal groups[1,21–24]. Given the miniature body size and the compact genome of *D. gyrociliatus*, we thus suggested that the molecular mechanisms controlling cell and organ growth might exhibit critical divergences in this lineage, should these two traits be connected. To test this, we used genome-wide KEGG annotation (Supplementary File 4) to reconstruct signalling pathways known to be involved in the control of cell growth and proliferation (cyclin/CDKs[71] and PI3K/Akt/mTOR[72]) and organ size (Hippo pathway[73]) in metazoans (Fig. 4a). *D. gyrociliatus* shows orthologues of all core components of these pathways (Supplementary Table 10), with the exception of PRR5—an mTOR complex 2 interactor that is, however, dispensable for complex integrity and/or kinase activity[74]—and a clear orthologue of p21/p27/p57 kinases, general inhibitors of cyclin-CDK complexes among other roles[75]. Besides, the Myc transduction pathway, which regulates growth and proliferation[76] and sits downstream of the Hippo and PI3K/Akt/mTOR pathways[73,77], lacks the regulators *mad* (in *D. gyrociliatus*) and *mnt* (in all Dinophilidae), a condition also shared with the appendicularian *O. dioica* (Fig. 4b and Supplementary Table 11). In Dinophilidae, MYC additionally has a W135 point mutation in the broadly conserved MYC box II (MBII) transactivation domain that has been shown to impair MYC function in human cells, in particular its ability to repress growth arrest genes[78] (Fig. 4c). Myc downregulation in vertebrates and flies causes hypoplasia[79], which could explain the miniature size of dinophilids, and slows down DNA replication[80], which could act as a selective pressure favouring smaller genomes. Although the full extent of these genomic changes is hard to evaluate given the poor understanding of cell and organ growth in annelids, our data provide a substrate for studying whether there is a mechanistic link between genome size reduction and organism miniaturization in *D. gyrociliatus*.

To investigate how compaction affected genome regulation, we first used assay for transposase-accessible chromatin using

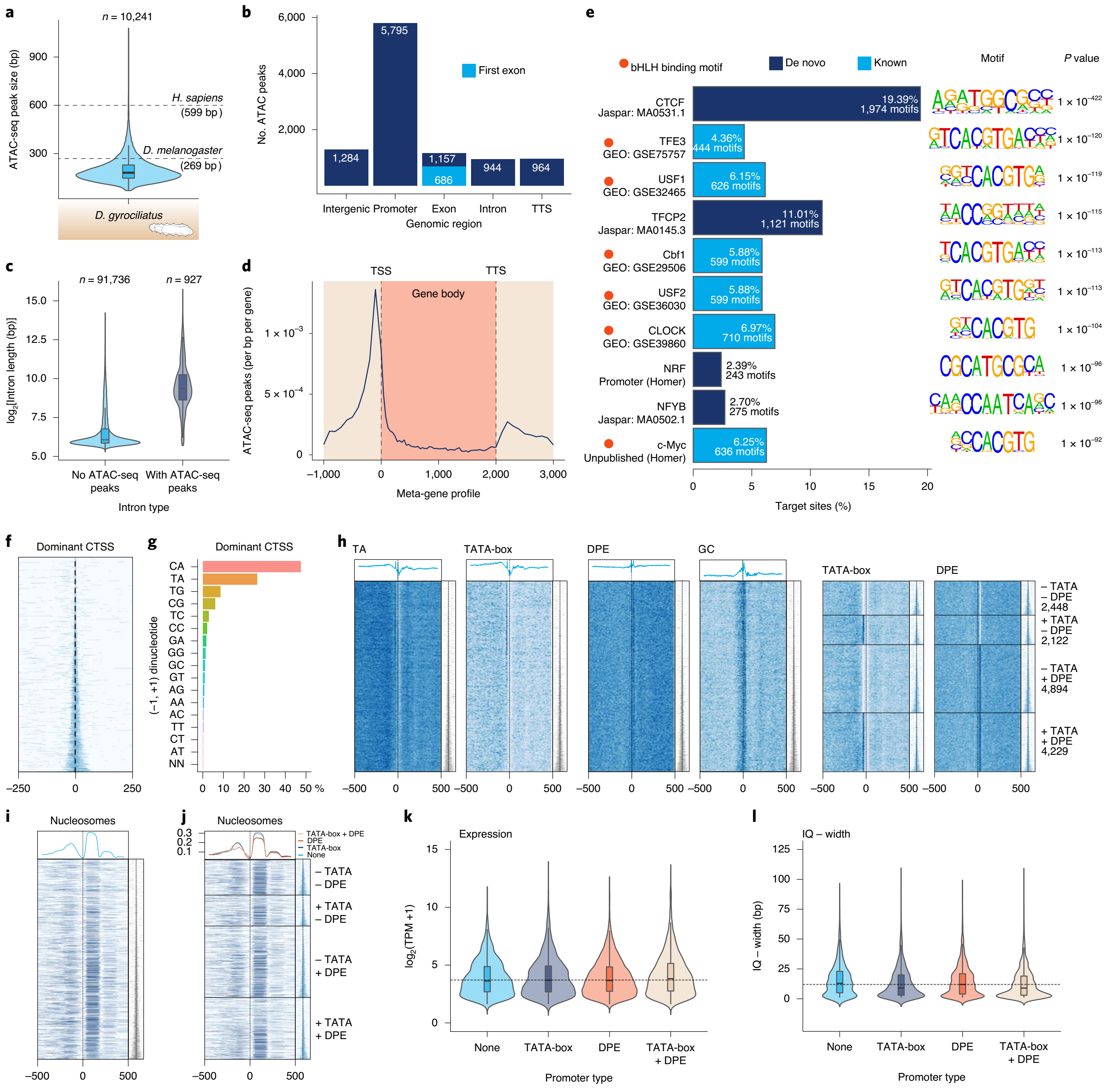

Fig. 5 | The regulatory genomic landscape of *D. gyrociliatus*. **a**, Violin plot depicting ATAC-seq peak size distribution in *D. gyrociliatus* compared to the median values in the fly *D. melanogaster* and humans. The open chromatin regions are shorter in *D. gyrociliatus* than in other animal genomes. **b**, Distribution of ATAC-seq peaks according to genomic feature. Most of the open chromatin regions are found in promoters, intergenic regions and (first) introns. **c**, Violin plots of size distributions in introns with and without ATAC-seq peaks. The presence/absence of open chromatin regions in introns correlates positively with size. **d**, Metagene profile of ATAC-seq signal. All gene lengths are adjusted to 2 kb. **e**, Top ten most-significant motifs identified in *D. gyrociliatus* ATAC-seq peaks. The most abundant motif in open chromatin regions corresponds to CTCF. **f**,**g**, Tag clusters centred on the dominant CAGE-supported TSS (CTSS) are usually narrow (based on interquantile range q0.1–q0.9) (**f**) and retain the canonical metazoan polymerase II initiation pyrimidine (C, T)/purine (A, G) dinucleotides (**g**). **h**, Most (11,245 out of 13,693) of the CTSS have a TATA-box and/or a downstream promoter element (DPE). **i**,**j**, Nucleosomes are consistently located after the CTSS (**i**), regardless of the promoter type (**j**). **k**,**l**, While genes with a TATA-box tend to be slightly narrower on average (**l**), there are no major differences in expression levels between genes with different promoter elements (**k**).

sequencing (ATAC-seq) to identify ~10,000 reproducible open chromatin regions in adult *D. gyrociliatus* females (Extended Data Fig. 9a–d). Open chromatin regions are short in *D. gyrociliatus* and mostly found in promoters (Fig. 5a,b), consistent with its small genome size and small intergenic regions. Despite the generally short intron size in *D. gyrociliatus*, 944 ATAC-seq peaks were in intronic regions substantially larger than non-regulatory introns (Fig. 5c). We recovered a canonical regulatory profile (Fig. 5d), which together with the lack of putative spliced leaders in 5′ UTRs (Extended Data Fig. 4g), suggests that *trans*-splicing and operons

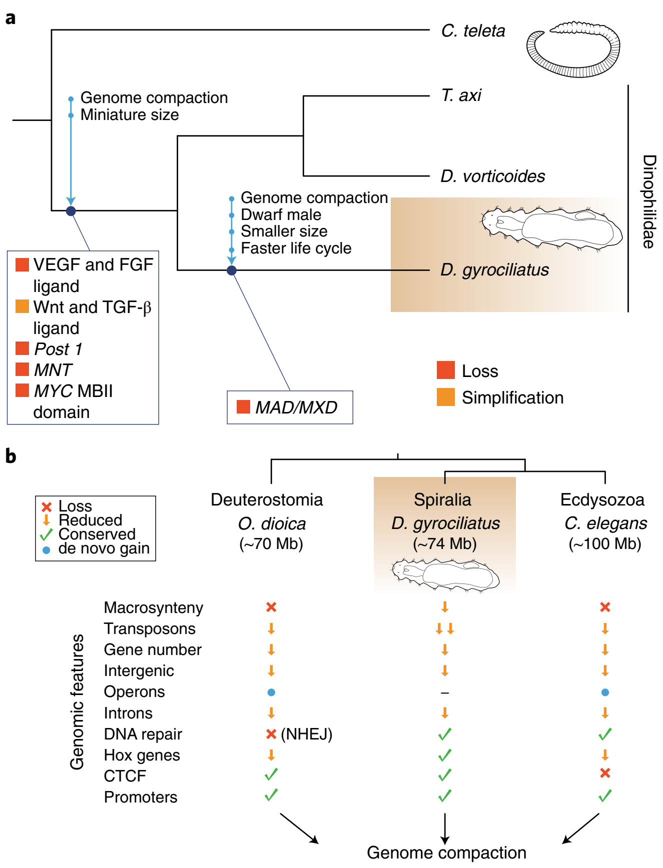

Fig. 6 | A new conservative route to genome compaction in *D. gyrociliatus*. **a**, Schematic diagram of the genomic changes which occurred during genome compaction and morphological miniaturization in *D. gyrociliatus* and Dinophilidae. **b**, *D. gyrociliatus* genome represents a more conservative evolutionary pathway to genome compaction compared to the more drastic genomic changes experienced by other bilaterian lineages with compact genomes, such as *O. dioica* and *C. elegans*.

do not occur in *D. gyrociliatus*, similar to other annelids[81]. The CTCF DNA-binding motif was the most abundant in active regulatory regions, located mostly in promoters and as single motifs (Fig. 5e and Extended Data Fig. 9e–h). Unlike nematodes with compact genomes[82], which lack CTCF, the *D. gyrociliatus* genome encodes for a CTCF orthologue (Supplementary Fig. 8). However, localization of CTCF DNA-binding motifs, for the most part close to transcriptional start sites, instead of in intergenic regions, suggests that CTCF might play a role in regulating gene expression in *D. gyrociliatus* rather than in chromatin architecture as seen in vertebrates[83]. Thus, our data indicate that *D. gyrociliatus* has retained conserved genomic regulatory features (for example, lack of operons and *trans*-splicing, and presence of CTCF) but streamlined regulatory regions and potentially lost distal intergenic *cis*-regulatory elements with genome compaction.

Since most regulatory information is restricted to promoter regions (<1 kilobase (kb) upstream of the transcription start site, TSS), we applied cap analyses gene expression (CAGE)-seq to characterize promoter architecture (Extended Data Fig. 10a). Promoters are narrow (<150 bp) in *D. gyrociliatus* and use pyrimidine–purine dinucleotides as preferred initiators (Fig. 5f,g and Extended Data Fig. 10e). Upstream TA and downstream GC enrichment, respectively, revealed the presence of TATA-box and downstream promoter elements (DPE) in *D. gyrociliatus*, with TATA-box generally associated with short promoters (Fig. 5h and Extended Data Fig. 10f). Similar to vertebrates[84], strength of nucleosome positioning correlates with promoter broadness in *D. gyrociliatus* (Fig. 5i) and thus narrow TATA-box dependent promoters have lower +1 nucleosome occupancy than wide non-TATA-box promoters (Fig. 5j). As in other eukaryotes, TATA-box containing *D. gyrociliatus* promoters have somewhat higher expression levels, while promoters with DPE motif have no particular features, indicating this element might be non-functional (Fig. 5k,l). Therefore, the general *D. gyrociliatus* promoter architecture resembles that of other bilaterians (Extended Data Fig. 10g), further supporting that genomic compaction did not alter genome regulation.

Discussion

Our study demonstrates that genome compaction and morphological miniaturization are specificities of *D. gyrociliatus* (Fig. 1e), grounded in a nested phylogenetic position within Annelida, TE depletion, intergenic region shortening, intron loss and streamlining of the gene complement and genome regulatory landscape (Fig. 2a,e, Fig. 3a and Fig. 5a,f). Traditionally, morphological miniaturization in *D. gyrociliatus* and Dinophiliformia has been considered a case of progenesis (underdevelopment)[45,52], yet the exact underlying mechanisms are unknown. As in other animal lineages[34,35,85], our data support that morphological change might be partially explained by gene loss in *D. gyrociliatus* (Fig. 6a), as we identified a reduced repertoire of extracellular signalling ligands and the loss of developmental genes related to missing organs, such as chaetae (*post1* and FGF ligand) and mesodermal derivatives like coeloms (VEGF ligand). However, *cis*-regulation of gene expression is mostly restricted to the proximal regions in *Dimorphilus* (Fig. 5b). Therefore, our study suggests that coordinated distal gene regulation, which is an animal innovation[86] whose emergence has been associated with the evolution of sophisticated gene regulatory landscapes and morphological diversification[87,88], is also limited in *D. gyrociliatus*.

Unlike in other cases of genomic compaction[5,30–33,36–39], but similar to what has been reported for the teleost fish *Takifugu rubripes*[89,90], our work provides compelling evidence that genome miniaturization did not trigger drastic changes in genome architecture and regulation in *D. gyrociliatus* (Fig. 3c, Fig. 5c,e,h and Fig. 6b). Therefore, the genomic features observed in appendicularians, tardigrades and some nematodes are lineage specificities that might have eventually facilitated genome compaction, but that are not always associated with genome size reduction, thus questioning the assumed causal link between fast-evolving genomic traits and genome compaction. Altogether, our study characterizes an alternative, more conservative route to genome compaction, and furthermore provides an exciting new system and genomic resources to investigate the evolutionary plasticity and function of core cellular mechanisms in animals.

Methods

Genome sequencing and assembly. Adult females of *D. gyrociliatus* were used to isolate genomic DNA following standard guanidium isothiocyanate protocol and RNase A treatment. Library was prepared using Pacific Biosciences 20-kb library preparation protocol and size-selected using BluePippin with 5-kb cutoff. The library was sequenced on a Pacific Bioscience RS II instrument using P6-C4 chemistry at the Norwegian Sequencing Centre. An Illumina library of median insert size of 298 bp was sequenced in 101 bases paired end mode on an Illumina HiSeq 2500 instrument at GeneCore (EMBL). All raw sequence data associated with this project are available under primary accession PRJEB37657 in the European Nucleotide Archive.

PacBio reads were filtered with SMRTAnalysis v.2.3.0.140936 and assembled with PBcR v.8.3rc2 (refs. [91,92]) using default options, except for *K*-mer = 14 and asmMerSize = 14. Four rounds of decontamination using Blobtools v.0.9.16 (ref. [93]) were applied, removing contigs with similarity to bacteria, algae, fungi or unicellular eukaryotes. A consensus assembly was generated with Quiver and improved with Pilon v.1.16 (ref. [94]) using the Illumina paired end reads previously filtered for adaptors with cutadapt v.1.4.2 (ref. [95]). We used HaploMerger2 v.20151124 (refs. [96,97]) to reconstruct a high-quality haploid reference assembly, which we further scaffolded with SSPACE-LongRead v.1.1 (ref. [98]).

We collected hundreds of adult individuals of *T. axi* Remane, 1925, at the intertidal beach of Königshafen, Sylt (Germany)[44] and extracted genomic DNA as described above to prepare a TruSeq v.3 Illumina library that was sequenced in 101 bases paired end mode on a full lane of an Illumina HiSeq 2500 instrument at GeneCore (EMBL). Before assembly, we removed adaptors and low-quality regions with cutadapt v.1.4.2 (ref. [95]) and Trimmomatic v.0.35 (ref. [99]), error correction with SPAdes v.3.6.2 (ref. [100]) and deduplication with Super_Deduper v.2.0. Cleaned reads were assembled with Platanus v.1.2.4 (ref. [101]) and contigs with similarity to proteobacteria were identified with Blobtools v.0.9.16 (ref. [93]). After removal of bacterial contigs, we generated the final assembly with Velvet v.1.2.10 (ref. [102]).

We used BUSCO v.2 pipeline (ref. [103]) to validate the completeness of the genome assemblies. Out of the 978 metazoan BUSCO genes, 930 were complete (95.1%), seven were fragmented (0.7%) and 41 were missing (4.2%) (Extended Data Fig. 1e) in the *D. gyrociliatus* genome assembly. Only 27 (2.8%) of the BUSCO genes were complete and duplicated. BUSCO analysis on the *T. axi* genome resulted in 835 complete (85.4%), 27 complete and duplicated (2.8%), 75 fragmented (7.7%) and 68 missing (6.9%) (Extended Data Fig. 1e). Finally, we used KAT v.2.4.2 (ref. [104]) to estimate the completeness and copy number variation of the assemblies (Supplementary Fig. 1).

Genome size measurements. For flow cytometry measures, adult *D. gyrociliatus* females and *C. elegans* worms (reference) were starved for 3–4 d before analysis. *D. gyrociliatus* and *C. elegans* were chopped with a razor blade in General-Purpose Buffer[105] and the resulting suspension of nuclei was filtered through a 30-µm nylon mesh and stained with propidium iodide (Sigma; $1\,\mathrm{mg\,ml^{-1}}$) on ice. We used a flow cytometer Partex CyFlow Space fitted with a Cobalt Samba green laser (532 nm, 100 mW) to analyse the samples, performing three independent runs with at least 5,000 nuclei per run. For *K*-mer-based measures, we used the raw Illumina paired end reads of *D. gyrociliatus* and *T. axi*. We removed adaptors using cutadapt v.1.4.271 (ref. [95]), quality trimmed the reads using Trimmomatic v.0.3575 (ref. [99]), performed error correction using SPAdes v.3.6.276 (ref. [100]) and removed duplicated reads using Super-Deduper v.2.0. We identified and removed contaminant reads using BlobTools v.1.1.1, and normalized read coverage to 100 times in both datasets using BBNorm from BBTools suite v.38.86 to mitigate the effects of a strong GC content bias in *D. gyrociliatus* and reduce the impact of highly abundant repeats in *T. axi*. We used Jellyfish v.2.2.386 (ref. [106]) to count and generate a histogram of canonical 31-mers, and GenomeScope 2.0 (refs. [107,108]) to estimate the genome size and heterozygosity (Fig. 1d and Supplementary Fig. 2). We also used Smudgeplot[107] to estimate ploidy and analyse the genome structure (Supplementary Fig. 3).

Transcriptome sequencing and assembly. A publicly available dataset (Sequence Read Archive (SRA), accession number SRX2030658) was used to generate a de novo transcriptome assembly as previously described[47]. Redundant contigs were removed using the cd-hit-est program with default parameters of CD-HIT (ref. [109]) and CAP3 (ref. [110]). Additionally, we used that dataset to generate a genome-guided assembly using Bowtie2 (ref. [111]) and Trinity v.2.1.1 (ref. [112]). Supplementary Table 2 shows standard statistics for the de novo and genome-guided assemblies calculated with Transrate[113]. Transcriptome completeness was evaluated with BUSCO v.2 (ref. [103]).

Stage-specific RNA-seq. Two biological replicates of four developmental stages of *D. gyrociliatus* (early embryo, 1–3-days-old; late embryo, 4–6-days-old; juvenile females, 7–9-days-old; and adult females, 20–23-days-old) were used to isolate total RNA with TRI Reagent Solution (Applied Biosystems) following manufacturer's recommendations and generate Illumina short-reads on a NextSeq 500 High platform in 75 base paired end reads mode and a ~270 bp library mean insert size at GeneCore (EMBL). We pseudo-aligned reads to *D. gyrociliatus* filtered gene models with Kallisto v.0.44.0 (ref. [114]), and followed the standard workflow of DESeq2 (ref. [115]) to estimate counts, calculate size factors, estimate the data dispersion, and perform a gene-level differential expression analysis between consecutive stages (Supplementary Data 1). Datasets were first corrected for low count and high dispersion values using the apeglm log-fold change shrinkage estimator[116], and then compared using Wald tests between contrasts. For clustering and visualization, we homogenized the variance across expression ranks by applying a variance-stabilizing transformation to the DESeq2 datasets. We used the pheatmap package to create heatmaps[117], the package EnhancedVolcano for volcano plots[118] and ggplot2 for the remaining plots[119]. To characterize and identify enriched gene ontology terms, we used the package clusterProfiler[120]. All analyses were performed in R (ref. [121]) using the RStudio Desktop[122].

Phylogenetic analysis. Annelid transcriptomes (Supplementary Data 1) were downloaded from SRA and assembled using Trinity v.2.5.1 (ref. [112]) with the Trimmomatic[99] read trimming option. Transcriptomes were then translated using Transdecoder v.5.0.2 (ref. [112]) after searching for similarity against the metazoan Swissprot database. Predicted proteins were searched using HMMER[123] for 1,148 single-copy phylogenetic markers previously described[124] using reciprocal BLAST to discard possible paralogues and character supermatrix was assembled as described before[124]. From this initial dataset, we selected the 264 genes with lowest saturation, yielding a concatenate alignment of 71,508 positions (as the analysis of the full dataset with site-heterogeneous models was not computationally tractable). Phylogenetic analyses were performed on the concatenated alignment using IQTREE[125] with a C60 mixture model, an LG matrix to account for transition rates within each profile, the FreeRate heterogeneity model (R4) to describe across sites evolution rates, and an optimization of amino acid frequencies using maximum likelihood. Support values were drawn from 1,000 ultrafast bootstraps with NNI optimization. We also carried out Bayesian reconstruction using a site-heterogeneous CAT + GTR + Gamma model running two chains for <1,000 iterations. We reached reasonable convergence for one of the datasets (bpdiff > 0.19).

Annotation of repeats and transposable elements. We used RepeatModeler v.1.0.4 9 (ref. [126]) and RepeatMasker 'open-4.0' (ref. [126]) to generate an automated annotation of TEs and repeats (Supplementary Table 3). We performed a BLAST analysis using the TE sequences recovered with RepeatModeler and PFAM sequence collections corresponding to entries RVT_1 (PF00078) (Supplementary Table 4) to uncover non-LTR retrotransposons and Helitrons represented by only a few copies. Using MITE Digger[127], we identified MITEs whose terminal inverted repeats matched *Mariner* transposons in the *D. gyrociliatus* genome. *D. gyrociliatus* DNA transposons belong to *Mariner* and *Mutator-Like Elements* (*MULE*) on the basis of the amino acid signature of their transposases. To establish the gene arrangement in LTR retrotransposons, we performed six-frame translations of most intact copies, identified as such by having two identical LTRs and being flanked by short direct repeats created by target site duplication. LTR retrotransposons were further compared to other elements of the *Ty3/gypsy* clade using a set of protein sequences comprising the reverse transcriptase domain and the integrase core domain. The phylogeny of *Ty3/gypsy* was established with a collection of sequences from the Gypsy database[128], including hits obtained with TBLASTN (databases NR and TSA) using *D. gyrociliatus* sequences as queries. To look for distant homologues of the protein found downstream from the integrase in LTR retrotransposons, we submitted a multiple sequence alignment of ten peptide sequences (corrected to the original coding frame when recovered from disrupted genes) to HHPred (database PDB_mmCIF70_28_Dec). Using MODELLER, the three best hits ($P > 99$, E value $< e^{-29}$) were used to model the three-dimensional structure of the *Dingle-1* envelope.

Gene prediction and functional annotation. The predicted set of core eukaryotic genes generated by CEGMA[129] was used to train and run AUGUSTUS v.3.2.1 (ref. [130]). The predicted proteomes of the annelids *C. teleta* and *H. robusta* were aligned to the *D. gyrociliatus* genome using EXONERATE v.2.2.0 (ref. [131]) and PASA v.2.0.2 (ref. [132]) was used to align the transcriptome to the genome with BLAT and GMAP aligners[133,134]. EvidenceModeler v.1.1.1 (ref. [135]) was used to generate weighted consensus gene predictions, giving a weight of 1 to ab initio gene predictions and spliced protein alignments, and a weight of 10 to the PASA transcript assemblies. EvidenceModeler output was used to refine PASA gene models and generate alternative splice variants. Predictions with BLAST hit against transposons and/or with an overlap ≥90% on masked regions were removed. The final prediction set contains 14,203 coding-protein loci that generate 17,409 different peptides. We used ORFik[136] to refine TSS with CAGE-seq data. Functional annotation for the 17,409 different transcripts was performed with Trinotate v.3.0. We retrieved a functional annotation for 13,437 gene models (77.18%).

Gene structure evolution. We compared genome-wide values of gene structure parameters among *D. gyrociliatus*, *C. teleta*, *H. robusta*, *D. melanogaster*, *C. elegans* and *O. dioica* (Supplementary Table 6). To identify splice leader sequences in *D. gyrociliatus*, we predicted protein-coding sequences in the de novo assembled transcriptome with Transdecoder v.5.5.0 (ref. [112]) and used the scripts nr_ORFs_gff3.pl (from Transdecoder) and gff3_file_UTR_seq_extractor.pl (from PASA) to extract the non-redundant 5′ UTR sequences of protein-coding transcripts. We used these sequences and Jellyfish v.2.2.3 (ref. [106]) to identify over-represented 22-mer and 50-mer sequences that would correspond to the splice leader.

Intron evolution analysis. We compared distributions of intron lengths between *D. gyrociliatus*, *Homo sapiens*, *C. teleta*, *Crassostrea gigas*, *Lottia gigantea*, *Strigamia maritima* and *Branchiostoma lanceolatum* (Supplementary Table 6) using only introns in genes with orthologues across the seven species (as defined by OrthoFinder; see below) and orthogroups with less than four paralogues per species. To identify conserved and new *D. gyrociliatus* introns, we aligned each *D. gyrociliatus* protein against each annotated protein isoform of each orthologous gene of the abovementioned six species and added the intron positions into the alignments[137]. To identify high-confidence conserved intron positions, we required that a given *D. gyrociliatus* intron position was found at the exact position of the alignment and with the same phase (0, 1 or 2) in at least four out of six other species. To define high-confidence non-conserved (probably new) introns, we required that a *D. gyrociliatus* intron position did not match an intron position with the same phase within 25 alignment positions in any of the other six species. To assess the impact of intron length on splicing efficiency on *D. gyrociliatus*, *S. maritima* and *H. sapiens*, we used RNA-seq-based quantifications of intron retention as previous described[138] and implemented by vast-tools[139]. Only introns that had sufficient read coverage[138,139] were used to calculate average PIR.

To quantify intron gain and loss in *D. gyrociliatus* we generated a database of homologous introns from 28 metazoan genomes (Supplementary Table 6), obtaining one-to-one orthologous genes using BUSCO v.3 (ref. [103]) (prot mode and 1×10^{-4} *E* value) and the OrthoDB v.9 (ref. [140]) dataset of 978 single-copy animal orthologues. We aligned the predicted peptides using MAFFT v.7.310 G-INS-i algorithm[141] and used Malin[142] to identify conserved intron sites and infer their conservation status in ancestral nodes. We estimated the rates of intron gain and loss in each node with Malin's built-in model maximum-likelihood optimization procedure. We used this model to estimate the posterior probabilities of intron presence, gain and loss in extant and ancestral nodes. For each node, we calculated the intron density expressed as introns per kb of coding sequence (introns per CDS kb), as follows:

$$\text{intron density}_i = ((\text{num introns}_i/\text{num genes})/\text{median gene length})^*1,000$$

where num introns_i is the number of introns present in a given node (extant or ancestral, corrected by missing sites), num genes = 978 (number of alignments of one-to-one orthologues) and median gene length = 682.5 bp (as obtained from the lengths of the seed proteins curated in the OrthoDB v.9 Metazoa dataset; 'ancestral' FASTA file). We used the same strategy to obtain the rates of intron gain and loss per node in terms of introns per CDS kb. In addition, we inferred the uncertainty of the estimated intron gains, losses and presence values with Malin and 1,000 bootstrap iterations. To visualize the evolution of intron content, we used the ape library v.5.0 (ref. [143]) from the R statistical package v.3.6 (ref. [121]). To calculate the percentage of ancestral metazoan introns retained in each species, we retrieved all introns present in the last common metazoan ancestor (at >99% probability, $n =$ 3,024) and calculated the sum of their presence probabilities in extant species.

Gene family evolution analyses. We used OrthoFinder v.2.2.7 (ref. [144]) with default values to reconstruct clusters of orthologous genes between *D. gyrociliatus* and 27 other animal proteomes (Supplementary Table 6). OrthoFinder gene families were used to infer gene family gains and losses at different nodes using the ETE 3 library[145]. Gene expansions were computed for each species using a hypergeometric test against the median gene number per species for a given family. We used the functionally annotated gene sets of *D. gyrociliatus*, *C. teleta* and *H. robusta* to identify their repertoires of transcription factors, ligands and receptors. If a gene was not in the annotated *D. gyrociliatus* genome assembly, we performed manual search via BLAST on the de novo and genome-guided transcriptome. For *T. axi* and *D. vorticoides*, gene identification was conducted on the assembled transcriptome via manual BLAST searches. To reconstruct KEGG pathways via KEGG Mapper[146], we used the functional annotations obtained from Trinotate to extract KEGG IDs. GPCR sequences in *D. gyrociliatus* and other animals (Supplementary Table 7) were retrieved using HMMER v.3.2.1 (refs. [123,147]) (*E* value cutoff < 0.01) with Pfam profiles of class A (PF00001), class B (PF00002), class C (PF00003) and class F (PF01534) GPCRs (according to GRAFS classification). Sequences from each class were tested for false positives from other classes (including cAMP slime-mold class E GPCRs, PF05462). Phylogenetic analyses of GPCRs were performed as described elsewhere[148]. Neuropeptide candidates (Supplementary Data 2) were retrieved by a combination of BLAST searches (*E* value cutoff < 0.1) and the use of a customized script[148] to detect cleavage patterns on precursors.

Orthology assignment. Multiple protein alignments were constructed with MAFFT v.7 (ref. [141]); poorly aligned regions were either removed by hand or with gBlocks[149]. Maximum likelihood trees were constructed with FastTree 2 (ref. [150]) using default parameters and visualized with FigTree.

Gene expression analyses. *D. gyrociliatus* embryos were collected in their egg clusters and manually dissected. The embryonic eggshell was digested in a solution of 1% sodium thioglycolate (Sigma-Aldrich, T0632) and 0.05% protease (Sigma-Aldrich, P5147) in seawater, pH 8, for 30 min at room temperature, followed by relaxation in $MgCl_2$ and fixation. Whole-mount in situ hybridization (WMISH) was performed as described elsewhere[47]. Images were taken with a Zeiss Axiocam HRc connected to a Zeiss Axioscope Ax10 using bright-field Nomarski optics. *C. teleta* embryos were fixed and WMISH was performed as previously described[151]. *C. teleta* orthologues *Ct-fgf8/17/18/24* (ref. [152]) (protein ID: 218971), *Ct-pvf1* (ref. [153]) (protein ID: 153454) and *Ct-pvf2* (ref. [153]) (protein ID: 220370) were mined from the publicly available genome[50]. WMISH samples were imaged on a Leica DMRA2 compound microscope coupled with a QIClick camera. Animals stained for F-actin were fixed for 30 min at room temperature, incubated with 1:100 BODIPY FL-Phallacidin (Life Technologies, catalogue no. B607) and imaged with an IXplore SpinSR (Olympus). *Capitella* WMISH images were rendered using Helicon Focus (HelSoft). Contrast and brightness of images were edited with Photoshop (Adobe Systems) when needed.

Macrosynteny analysis. Single-copy orthologues obtained using the mutual best hit approach were used to generate Oxford synteny plots comparing sequentially indexed orthologue positions as previously described[154]. Plotting order was determine by hierarchical clustering of the shared orthologue content using the complete linkage method[155].

ATAC-seq. ATAC-seq libraries were performed as described elsewhere[156], using 50,000–70,000 cells (~18 adult females). Cell dissociation and lysis was improved by disaggregating the tissue with a syringe in lysis buffer. Transposed DNA fragments were amplified by 16 cycles of PCR. Two biological replicates were sequenced in an Illumina NextSeq500 in rapid paired end mode and 75 base read length. Adaptor contamination was removed with cutadapt v.1.2.1 (ref. [95]) and cleaned reads were aligned to the unmasked genome with bowtie2 (ref. [111]). Peaks were called with MACS2 v.2.1.1.20160309 (ref. [157]) with the options --nomodel --extsize 70 --shift -30 --call-summits --keep-dup 1. Irreproducible discovery rates (IDR) were calculated with IDRCode[158]. A final set of 10,241 consistent peaks (IDR ≤ 0.05) was used for de novo motif enrichment analysis using HOMER[159], with default parameters, except -size given (Supplementary Data 1).

CAGE-seq. Total RNA from adult *D. gyrociliatus* was isolated using Trizol followed by RNeasy RNA clean-up protocol (Qiagen). CAGE libraries were prepared for two biological replicates (barcodes ATG and TAC) using the latest nAnT-iCAGE protocol[160]. The libraries were sequenced in single-end 50 base mode (Genomic Facility, MRC LMS). Demultiplexed CAGE reads (47 bp) were mapped to the *D. gyrociliatus* genome assembly using Bowtie2 (ref. [111]) and resulting Bam files were imported into R using the standard CAGEr package (v.1.20.0) and G-correction workflow[161]. Normalization was performed using a referent power-law distribution[162] and CAGE-derived TSSs that passed the threshold of 1 transcript per million (TPM) were clustered together using distance-based clustering (Supplementary Data 1). Genomic locations of tag clusters were determined using the ChIPseeker package and gene model annotations, where promoters were defined to include 500 bp upstream and 100 bp downstream of the annotated transcript start site. Visualization of motifs, sequence patterns or reads coverage was performed using Heatmaps and seqPattern Bioconductor packages.

Reporting Summary. Further information on research design is available in the Nature Research Reporting Summary linked to this article.

Data availability

All new raw sequence data associated with this project are available under primary accession PRJEB37657 in the European Nucleotide Archive. Genome annotation files and additional datasets are available in https://github.com/ChemaMD/DimorphilusGenome.

Code availability

All custom code used in this study is freely available in https://github.com/fmarletaz/comp_genomics.

Received: 21 April 2020; Accepted: 15 September 2020;
Published online: 16 November 2020

References

1. Gregory, T. R. in *The Evolution of the Genome* (ed. Gregory, T. R.) 3–87 (Academic Press, 2005).
2. Gregory, T. R. Coincidence, coevolution, or causation? DNA content, cellsize, and the C-value enigma. *Biol. Rev.* **76**, 65–101 (2001).
3. Blommaert, J., Riss, S., Hecox-Lea, B., Mark Welch, D. B. & Stelzer, C. P. Small, but surprisingly repetitive genomes: transposon expansion and not polyploidy has driven a doubling in genome size in a metazoan species complex. *BMC Genomics* **20**, 466 (2019).
4. Sun, C. et al. LTR retrotransposons contribute to genomic gigantism in plethodontid salamanders. *Genome Biol. Evol.* **4**, 168–183 (2012).
5. Naville, M. et al. Massive changes of genome size driven by expansions of non-autonomous transposable elements. *Curr. Biol.* **29**, 1161–1168 (2019).
6. Talla, V. et al. Rapid increase in genome size as a consequence of transposable element hyperactivity in wood-white (Leptidea) butterflies. *Genome Biol. Evol.* **9**, 2491–2505 (2017).
7. Ohno, S. *Evolution by Gene Duplication* (Springer, 1970).
8. Sacerdot, C., Louis, A., Bon, C., Berthelot, C. & Roest Crollius, H. Chromosome evolution at the origin of the ancestral vertebrate genome. *Genome Biol.* **19**, 166 (2018).
9. Braasch, I. & Postlethwait, J. H. in *Polyploidy and Genome Evolution* (eds Soltis, P. S. & Soltis, D. E.) 341–383 (Springer, 2012).
10. Li, Z. et al. Multiple large-scale gene and genome duplications during the evolution of hexapods. *Proc. Natl Acad. Sci. USA* **115**, 4713–4718 (2018).
11. Sotero-Caio, C. G., Platt, R. N. 2nd, Suh, A. & Ray, D. A. Evolution and diversity of transposable elements in vertebrate genomes. *Genome Biol. Evol.* **9**, 161–177 (2017).
12. Kapusta, A. & Suh, A. Evolution of bird genomes—a transposon's-eye view. *Ann. NY Acad. Sci.* **1389**, 164–185 (2017).

13. Kapusta, A., Suh, A. & Feschotte, C. Dynamics of genome size evolution in birds and mammals. *Proc. Natl Acad. Sci. USA* **114**, E1460–E1469 (2017).
14. Robertson, F. M. et al. Lineage-specific rediploidization is a mechanism to explain time-lags between genome duplication and evolutionary diversification. *Genome Biol.* **18**, 111 (2017).
15. Lynch, M. & Conery, J. S. The origins of genome complexity. *Science* **302**, 1401–1404 (2003).
16. Lynch, M. *The Origins of Genome Architecture* (Sinauer Associates, 2007).
17. Sundaram, V. & Wysocka, J. Transposable elements as a potent source of diverse *cis*-regulatory sequences in mammalian genomes. *Philos. Trans. R. Soc. Lond. B* **375**, 20190347 (2020).
18. Feschotte, C. Transposable elements and the evolution of regulatory networks. *Nat. Rev. Genet.* **9**, 397–405 (2008).
19. Kozlowski, J., Konarzewski, M. & Gawelczyk, A. T. Cell size as a link between noncoding DNA and metabolic rate scaling. *Proc. Natl Acad. Sci. USA* **100**, 14080–14085 (2003).
20. Pagel, M. & Johnstone, R. A. Variation across species in the size of the nuclear genome supports the junk-DNA explanation for the C-value paradox. *Proc. Biol. Sci.* **249**, 119–124 (1992).
21. Cavalier-Smith, T. Economy, speed and size matter: evolutionary forces driving nuclear genome miniaturization and expansion. *Ann. Bot.* **95**, 147–175 (2005).
22. Gregory, T. R., Hebert, P. D. N. & Kolasa, J. Evolutionary implications of the relationship between genome size and body size in flatworms and copepods. *Heredity* **84**, 201–208 (2000).
23. Finston, T. L., Hebert, P. D. N. & Foottit, R. B. Genome size variation in aphids. *Insect Biochem. Mol. Biol.* **25**, 189–196 (1995).
24. Hinegardner, R. Cellular DNA content of the Mollusca. *Comp. Biochem. Physiol. A* **47**, 447–460 (1974).
25. Wright, N. A., Gregory, T. R. & Witt, C. C. Metabolic 'engines' of flight drive genome size reduction in birds. *Proc. Biol. Sci.* **281**, 20132780 (2014).
26. Abad, P. et al. Genome sequence of the metazoan plant-parasitic nematode *Meloidogyne incognita*. *Nat. Biotechnol.* **26**, 909–915 (2008).
27. International Helminth Genomes Consortium. Comparative genomics of the major parasitic worms. *Nat. Genet.* **51**, 163–174 (2019).
28. Slyusarev, G. S., Starunov, V. V., Bondarenko, A. S., Zorina, N. A. & Bondarenko, N. I. Extreme genome and nervous system streamlining in the invertebrate parasite *Intoshia variabili*. *Curr. Biol.* **30**, 1292–1298 (2020).
29. Sharko, F. S. et al. A partial genome assembly of the miniature parasitoid wasp, *Megaphragma amalphitanum*. *PLoS ONE* **14**, e0226485 (2019).
30. C. elegans Sequencing Consortium. Genome sequence of the nematode *C. elegans*: a platform for investigating biology. *Science* **282**, 2012–2018 (1998).
31. Hashimoto, T. et al. Extremotolerant tardigrade genome and improved radiotolerance of human cultured cells by tardigrade-unique protein. *Nat. Commun.* **7**, 12808 (2016).
32. Yoshida, Y. et al. Comparative genomics of the tardigrades *Hypsibius dujardini* and *Ramazzottius varieornatus*. *PLoS Biol.* **15**, e2002266 (2017).
33. Seo, H. C. et al. Miniature genome in the marine chordate *Oikopleura dioica*. *Science* **294**, 2506 (2001).
34. Fernández, R. & Gabaldón, T. Gene gain and loss across the metazoan tree of life. *Nat. Ecol. Evol.* **4**, 524–533 (2020).
35. Guijarro-Clarke, C., Holland, P. W. H. & Paps, J. Widespread patterns of gene loss in the evolution of the animal kingdom. *Nat. Ecol. Evol.* **4**, 519–523 (2020).
36. Denoeud, F. et al. Plasticity of animal genome architecture unmasked by rapid evolution of a pelagic tunicate. *Science* **330**, 1381–1385 (2010).
37. Ganot, P., Kallesoe, T., Reinhardt, R., Chourrout, D. & Thompson, E. M. Spliced-leader RNA trans splicing in a chordate, *Oikopleura dioica*, with a compact genome. *Mol. Cell. Biol.* **24**, 7795–7805 (2004).
38. Guiliano, D. B. & Blaxter, M. L. Operon conservation and the evolution of *trans*-splicing in the phylum Nematoda. *PLoS Genet.* **2**, e198 (2006).
39. Danks, G. B. et al. *Trans*-splicing and operons in metazoans: translational control in maternally regulated development and recovery from growth arrest. *Mol. Biol. Evol.* **32**, 585–599 (2015).
40. Dieterich, C. et al. The *Pristionchus pacificus* genome provides a unique perspective on nematode lifestyle and parasitism. *Nat. Genet.* **40**, 1193–1198 (2008).
41. Gambi, M. C., Ramella, L., Sella, G., Protto, P. & Aldieri, E. Variation in genome size in benthic Polychaetes: systematic and ecological relationships. *J. Mar. Biol. Assoc. UK* **77**, 1045–1057 (1997).
42. Gregory, T. R. et al. Eukaryotic genome size databases. *Nucleic Acids Res.* **35**, D332–D338 (2007).
43. Simonini, R., Molinari, F., Pagliai, A. M., Ansaloni, I. & Prevedelli, D. Karyotype and sex determination in *Dinophilus gyrociliatus* (Polychaeta: Dinophilidae). *Mar. Biol.* **142**, 441–445 (2003).
44. Worsaae, K., Kerbl, A., Vang, A. & Gonzalez, B. C. Broad North Atlantic distribution of a meiobenthic annelid—against all odds. *Sci. Rep.* **9**, 15497 (2019).
45. Kerbl, A., Fofanova, E. G., Mayorova, T. D., Voronezhskaya, E. E. & Worsaae, K. Comparison of neuromuscular development in two dinophilid species (Annelida) suggests progenetic origin of *Dinophilus gyrociliatus*. *Front. Zool.* **13**, 49 (2016).
46. Windoffer, R. & Westheide, W. The nervous system of the male *Dinophilus gyrociliatus* (Annelida: Polychaeta). I. Number, types and distribution pattern of sensory cells. *Acta Zool.* **69**, 55–64 (1988).
47. Kerbl, A., Martin-Duran, J. M., Worsaae, K. & Hejnol, A. Molecular regionalization in the compact brain of the meiofaunal annelid *Dinophilus gyrociliatus* (Dinophilidae). *EvoDevo* **7**, 20 (2016).
48. Kerbl, A., Conzelmann, M., Jekely, G. & Worsaae, K. High diversity in neuropeptide immunoreactivity patterns among three closely related species of Dinophilidae (Annelida). *J. Comp. Neurol.* **525**, 3596–3635 (2017).
49. Nelson, J. A. The early development of *Dinophilus*: a study in cell-lineage. *Proc. Natl Acad. Sci. USA* **56**, 687–737 (1904).
50. Simakov, O. et al. Insights into bilaterian evolution from three spiralian genomes. *Nature* **493**, 526–531 (2013).
51. Hermans, C. O. The systematic position of the Archiannelida. *Syst. Zool.* **18**, 85–102 (1969).
52. Struck, T. H. et al. The evolution of annelids reveals two adaptive routes to the interstitial realm. *Curr. Biol.* **25**, 1993–1999 (2015).
53. Andrade, S. C. et al. Articulating 'archiannelids': phylogenomics and annelid relationships, with emphasis on meiofaunal taxa. *Mol. Biol. Evol.* **32**, 2860–2875 (2015).
54. Helm, C. et al. Convergent evolution of the ladder-like ventral nerve cord in Annelida. *Front. Zool.* **15**, 36 (2018).
55. Malik, H. S., Henikoff, S. & Eickbush, T. H. Poised for contagion: evolutionary origins of the infectious abilities of invertebrate retroviruses. *Genome Res.* **10**, 1307–1318 (2000).
56. Stevens, L. et al. Comparative genomics of 10 new *Caenorhabditis* species. *Evol. Lett.* **3**, 217–236 (2019).
57. Stevens, L. et al. The genome of *Caenorhabditis bovis*. *Curr. Biol.* **30**, 1023–1031 (2020).
58. Fredriksson, R. & Schioth, H. B. The repertoire of G-protein-coupled receptors in fully sequenced genomes. *Mol. Pharmacol.* **67**, 1414–1425 (2005).
59. Boothby, T. C. et al. Evidence for extensive horizontal gene transfer from the draft genome of a tardigrade. *Proc. Natl Acad. Sci. USA* **112**, 15976–15981 (2015).
60. Seo, H. C. et al. *Hox* cluster disintegration with persistent anteroposterior order of expression in *Oikopleura dioica*. *Nature* **431**, 67–71 (2004).
61. Hui, J. H. et al. Extensive chordate and annelid macrosynteny reveals ancestral homeobox gene organization. *Mol. Biol. Evol.* **29**, 157–165 (2012).
62. Frobius, A. C., Matus, D. Q. & Seaver, E. C. Genomic organization and expression demonstrate spatial and temporal Hox gene colinearity in the lophotrochozoan *Capitella* sp. I. *PLoS ONE* **3**, e4004 (2008).
63. Schiemann, S. M. et al. Clustered brachiopod Hox genes are not expressed collinearly and are associated with lophotrochozoan novelties. *Proc. Natl Acad. Sci. USA* **114**, E1913–E1922 (2017).
64. Martin-Duran, J. M., Passamaneck, Y. J., Martindale, M. Q. & Hejnol, A. The developmental basis for the recurrent evolution of deuterostomy and protostomy. *Nat. Ecol. Evol.* **1**, 0005 (2016).
65. Fischer, A. H., Henrich, T. & Arendt, D. The normal development of *Platynereis dumerilii* (Nereididae, Annelida). *Front. Zool.* **7**, 31 (2010).
66. Seaver, E. C., Thamm, K. & Hill, S. D. Growth patterns during segmentation in the two polychaete annelids, *Capitella* sp. I and *Hydroides elegans*: comparisons at distinct life history stages. *Evol. Dev.* **7**, 312–326 (2005).
67. Duboule, D. The rise and fall of Hox gene clusters. *Development* **134**, 2549–2560 (2007).
68. Smith, F. W. et al. The compact body plan of tardigrades evolved by the loss of a large body region. *Curr. Biol.* **26**, 224–229 (2016).
69. Deng, W., Henriet, S. & Chourrout, D. Prevalence of mutation-prone microhomology-mediated end joining in a chordate lacking the c-NHEJ DNA repair pathway. *Curr. Biol.* **28**, 3337–3341 (2018).
70. Sekelsky, J. DNA Repair in *Drosophila*: mutagens, models, and missing genes. *Genetics* **205**, 471–490 (2017).
71. Satyanarayana, A. & Kaldis, P. Mammalian cell-cycle regulation: several Cdks, numerous cyclins and diverse compensatory mechanisms. *Oncogene* **28**, 2925–2939 (2009).
72. Kim, J. & Guan, K. L. mTOR as a central hub of nutrient signalling and cell growth. *Nat. Cell Biol.* **21**, 63–71 (2019).
73. Zhao, B., Tumaneng, K. & Guan, K. L. The Hippo pathway in organ size control, tissue regeneration and stem cell self-renewal. *Nat. Cell Biol.* **13**, 877–883 (2011).
74. Thedieck, K. et al. PRAS40 and PRR5-like protein are new mTOR interactors that regulate apoptosis. *PLoS ONE* **2**, e1217 (2007).
75. Coqueret, O. New roles for p21 and p27 cell-cycle inhibitors: a function for each cell compartment? *Trends Cell Biol.* **13**, 65–70 (2003).

76. Grandori, C., Cowley, S. M., James, L. P. & Eisenman, R. N. The Myc/Max/Mad network and the transcriptional control of cell behavior. *Annu. Rev. Cell Dev. Biol.* **16**, 653–699 (2000).
77. Mendoza, M. C., Er, E. E. & Blenis, J. The Ras-ERK and PI3K-mTOR pathways: cross-talk and compensation. *Trends Biochem. Sci.* **36**, 320–328 (2011).
78. Oster, S. K., Mao, D. Y., Kennedy, J. & Penn, L. Z. Functional analysis of the *N*-terminal domain of the Myc oncoprotein. *Oncogene* **22**, 1998–2010 (2003).
79. Trumpp, A. et al. c-Myc regulates mammalian body size by controlling cell number but not cell size. *Nature* **414**, 768–773 (2001).
80. Dominguez-Sola, D. et al. Non-transcriptional control of DNA replication by c-Myc. *Nature* **448**, 445–451 (2007).
81. Hastings, K. E. SL trans-splicing: easy come or easy go? *Trends Genet.* **21**, 240–247 (2005).
82. Heger, P., Marin, B. & Schierenberg, E. Loss of the insulator protein CTCF during nematode evolution. *BMC Mol. Biol.* **10**, 84 (2009).
83. Vietri Rudan, M. et al. Comparative Hi-C reveals that CTCF underlies evolution of chromosomal domain architecture. *Cell Rep.* **10**, 1297–1309 (2015).
84. Haberle, V. et al. Two independent transcription initiation codes overlap on vertebrate core promoters. *Nature* **507**, 381–385 (2014).
85. Albalat, R. & Cañestro, C. Evolution by gene loss. *Nat. Rev. Genet.* **17**, 379–391 (2016).
86. Sebe-Pedros, A. et al. The dynamic regulatory genome of *Capsaspora* and the origin of animal multicellularity. *Cell* **165**, 1224–1237 (2016).
87. Schwaiger, M. et al. Evolutionary conservation of the eumetazoan gene regulatory landscape. *Genome Res.* **24**, 639–650 (2014).
88. Villar, D., Flicek, P. & Odom, D. T. Evolution of transcription factor binding in metazoans—mechanisms and functional implications. *Nat. Rev. Genet.* **15**, 221–233 (2014).
89. Aparicio, S. et al. Whole-genome shotgun assembly and analysis of the genome of *Fugu rubripes*. *Science* **297**, 1301–1310 (2002).
90. Brenner, S. et al. Characterization of the pufferfish (*Fugu*) genome as a compact model vertebrate genome. *Nature* **366**, 265–268 (1993).
91. Berlin, K. et al. Assembling large genomes with single-molecule sequencing and locality-sensitive hashing. *Nat. Biotechnol.* **33**, 623–630 (2015).
92. Koren, S. et al. Hybrid error correction and de novo assembly of single-molecule sequencing reads. *Nat. Biotechnol.* **30**, 693–700 (2012).
93. Kumar, S., Jones, M., Koutsovoulos, G., Clarke, M. & Blaxter, M. Blobology: exploring raw genome data for contaminants, symbionts and parasites using taxon-annotated GC-coverage plots. *Front. Genet.* **4**, 237 (2013).
94. Walker, B. J. et al. Pilon: an integrated tool for comprehensive microbial variant detection and genome assembly improvement. *PLoS ONE* **9**, e112963 (2014).
95. Martin, M. Cutadapt removes adapter sequences from high-throughput sequencing reads. *EMBnet.journal* **17**, 10–12 (2011).
96. Huang, S. et al. HaploMerger: reconstructing allelic relationships for polymorphic diploid genome assemblies. *Genome Res.* **22**, 1581–1588 (2012).
97. Huang, S. et al. Decelerated genome evolution in modern vertebrates revealed by analysis of multiple lancelet genomes. *Nat. Commun.* **5**, 5896 (2014).
98. Boetzer, M. & Pirovano, W. SSPACE-LongRead: scaffolding bacterial draft genomes using long read sequence information. *BMC Bioinform.* **15**, 211 (2014).
99. Bolger, A. M., Lohse, M. & Usadel, B. Trimmomatic: a flexible trimmer for Illumina sequence data. *Bioinformatics* **30**, 2114–2120 (2014).
100. Bankevich, A. et al. SPAdes: a new genome assembly algorithm and its applications to single-cell sequencing. *J. Comput. Biol.* **19**, 455–477 (2012).
101. Kajitani, R. et al. Efficient *de novo* assembly of highly heterozygous genomes from whole-genome shotgun short reads. *Genome Res.* **24**, 1384–1395 (2014).
102. Zerbino, D. R. & Birney, E. Velvet: algorithms for de novo short read assembly using de Bruijn graphs. *Genome Res.* **18**, 821–829 (2008).
103. Simao, F. A., Waterhouse, R. M., Ioannidis, P., Kriventseva, E. V. & Zdobnov, E. M. BUSCO: assessing genome assembly and annotation completeness with single-copy orthologs. *Bioinformatics* **31**, 3210–3212 (2015).
104. Mapleson, D., Garcia Accinelli, G., Kettleborough, G., Wright, J. & Clavijo, B. J. KAT: a K-mer analysis toolkit to quality control NGS datasets and genome assemblies. *Bioinformatics* **33**, 574–576 (2016).
105. Pellicer, J. & Leitch, I. J. The application of flow cytometry for estimating genome size and ploidy level in plants. *Methods Mol. Biol.* **1115**, 279–307 (2014).
106. Marcais, G. & Kingsford, C. A fast, lock-free approach for efficient parallel counting of occurrences of k-mers. *Bioinformatics* **27**, 764–770 (2011).
107. Ranallo-Benavidez, T. R., Jaron, K. S. & Schatz, M. C. GenomeScope 2.0 and Smudgeplot for reference-free profiling of polyploid genomes. *Nat. Commun.* **11**, 1432 (2020).
108. Vurture, G. W. et al. GenomeScope: fast reference-free genome profiling from short reads. *Bioinformatics* **33**, 2202–2204 (2017).
109. Fu, L., Niu, B., Zhu, Z., Wu, S. & Li, W. CD-HIT: accelerated for clustering the next-generation sequencing data. *Bioinformatics* **28**, 3150–3152 (2012).
110. Huang, X. & Madan, A. CAP3: a DNA sequence assembly program. *Genome Res.* **9**, 868–877 (1999).
111. Langmead, B. & Salzberg, S. L. Fast gapped-read alignment with Bowtie 2. *Nat. Methods* **9**, 357–359 (2012).
112. Haas, B. J. et al. *De novo* transcript sequence reconstruction from RNA-seq using the Trinity platform for reference generation and analysis. *Nat. Protoc.* **8**, 1494–1512 (2013).
113. Smith-Unna, R., Boursnell, C., Patro, R., Hibberd, J. M. & Kelly, S. TransRate: reference-free quality assessment of de novo transcriptome assemblies. *Genome Res.* **26**, 1134–1144 (2016).
114. Bray, N. L., Pimentel, H., Melsted, P. & Pachter, L. Near-optimal probabilistic RNA-seq quantification. *Nat. Biotechnol.* **34**, 525–527 (2016).
115. Love, M. I., Huber, W. & Anders, S. Moderated estimation of fold change and dispersion for RNA-seq data with DESeq2. *Genome Biol.* **15**, 550 (2014).
116. Zhu, A., Ibrahim, J. G. & Love, M. I. Heavy-tailed prior distributions for sequence count data: removing the noise and preserving large differences. *Bioinformatics* **35**, 2084–2092 (2019).
117. Kolde, R. pheatmap: Pretty heatmaps. R package version 1.0.12 (2019).
118. Blighe, K., Rana, S. & Lewis, M. EnhancedVolcano: Publication-ready volcano plots with enhanced colouring and labeling. R package version 1.2.0 (2019).
119. Wickham, H. *ggplot2: Elegant Graphics for Data Analysis* (Springer, 2016).
120. Yu, G., Wang, L.-G., Han, Y. & He, Q.-Y. clusterProfiler: an R Package for comparing biological themes among gene clusters. *OMICS J. Integr. Biol.* **16**, 284–287 (2012).
121. R Core Team *R: A Language and Environment for Statistical Computing* (R Foundation for Statistical Computing, 2019).
122. *Integrated Development for R* (RStudio, 2019).
123. Eddy, S. R. Profile hidden Markov models. *Bioinformatics* **14**, 755–763 (1998).
124. Marletaz, F., Peijnenburg, K., Goto, T., Satoh, N. & Rokhsar, D. S. A new spiralian phylogeny places the enigmatic arrow worms among Gnathiferans. *Curr. Biol.* **29**, 312–318 (2019).
125. Nguyen, L. T., Schmidt, H. A., von Haeseler, A. & Minh, B. Q. IQ-TREE: a fast and effective stochastic algorithm for estimating maximum-likelihood phylogenies. *Mol. Biol. Evol.* **32**, 268–274 (2015).
126. Flynn, J. M. et al. RepeatModeler2 for automated genomic discovery of transposable element families. *Proc. Natl Acad. Sci. USA.* **117**, 9451–9457 (2020).
127. Yang, G. MITE Digger, an efficient and accurate algorithm for genome wide discovery of miniature inverted repeat transposable elements. *BMC Bioinform.* **14**, 186 (2013).
128. Llorens, C. et al. The Gypsy Database (GyDB) of mobile genetic elements: release 2.0. *Nucleic Acids Res.* **39**, D70–D74 (2011).
129. Parra, G., Bradnam, K. & Korf, I. CEGMA: a pipeline to accurately annotate core genes in eukaryotic genomes. *Bioinformatics* **23**, 1061–1067 (2007).
130. Stanke, M. & Waack, S. Gene prediction with a hidden Markov model and a new intron submodel. *Bioinformatics* **19**, ii215–ii225 (2003).
131. Slater, G. S. & Birney, E. Automated generation of heuristics for biological sequence comparison. *BMC Bioinform.* **6**, 31 (2005).
132. Haas, B. J. et al. Improving the *Arabidopsis* genome annotation using maximal transcript alignment assemblies. *Nucleic Acids Res.* **31**, 5654–5666 (2003).
133. Kent, W. J. BLAT—the BLAST-like alignment tool. *Genome Res.* **12**, 656–664 (2002).
134. Wu, T. D. & Watanabe, C. K. GMAP: a genomic mapping and alignment program for mRNA and EST sequences. *Bioinformatics* **21**, 1859–1875 (2005).
135. Haas, B. J. et al. Automated eukaryotic gene structure annotation using EVidenceModeler and the Program to Assemble Spliced Alignments. *Genome Biol.* **9**, R7 (2008).
136. Tjeldnes, H., Labun, K., Chyzynska, K., Torres Cleuren, Y. & Valen, E. ORFik: Open Reading Frames in Genomics. R package version 1.6.9 (2020).
137. Irimia, M. & Roy, S. W. Spliceosomal introns as tools for genomic and evolutionary analysis. *Nucleic Acids Res.* **36**, 1703–1712 (2008).
138. Braunschweig, U. et al. Widespread intron retention in mammals functionally tunes transcriptomes. *Genome Res.* **24**, 1774–1786 (2014).
139. Tapial, J. et al. An atlas of alternative splicing profiles and functional associations reveals new regulatory programs and genes that simultaneously express multiple major isoforms. *Genome Res.* **27**, 1759–1768 (2017).
140. Zdobnov, E. M. et al. OrthoDB v9.1: cataloging evolutionary and functional annotations for animal, fungal, plant, archaeal, bacterial and viral orthologs. *Nucleic Acids Res.* **45**, D744–D749 (2017).
141. Katoh, K. & Standley, D. M. MAFFT multiple sequence alignment software version 7: improvements in performance and usability. *Mol. Biol. Evol.* **30**, 772–780 (2013).
142. Csuros, M. Malin: maximum likelihood analysis of intron evolution in eukaryotes. *Bioinformatics* **24**, 1538–1539 (2008).

143. Paradis, E. & Schliep, K. ape 5.0: an environment for modern phylogenetics and evolutionary analyses in R. *Bioinformatics* **35**, 526–528 (2019).
144. Emms, D. M. & Kelly, S. OrthoFinder: phylogenetic orthology inference for comparative genomics. *Genome Biol.* **20**, 238 (2019).
145. Huerta-Cepas, J., Serra, F. & Bork, P. ETE 3: reconstruction, analysis, and visualization of phylogenomic data. *Mol. Biol. Evol.* **33**, 1635–1638 (2016).
146. Kanehisa, M. & Sato, Y. KEGG Mapper for inferring cellular functions from protein sequences. *Protein Sci.* **29**, 28–35 (2020).
147. Finn, R. D., Clements, J. & Eddy, S. R. HMMER web server: interactive sequence similarity searching. *Nucleic Acids Res.* **39**, W29–W37 (2011).
148. Thiel, D., Franz-Wachtel, M., Aguilera, F. & Hejnol, A. Xenacoelomorph neuropeptidomes reveal a major expansion of neuropeptide systems during early bilaterian evolution. *Mol. Biol. Evol.* **35**, 2528–2543 (2018).
149. Castresana, J. Selection of conserved blocks from multiple alignments for their use in phylogenetic analysis. *Mol. Biol. Evol.* **17**, 540–552 (2000).
150. Price, M. N., Dehal, P. S. & Arkin, A. P. FastTree 2—approximately maximum-likelihood trees for large alignments. *PLoS ONE* **5**, e9490 (2010).
151. Meyer, N. P., Carrillo-Baltodano, A., Moore, R. E. & Seaver, E. C. Nervous system development in lecithotrophic larval and juvenile stages of the annelid *Capitella teleta*. *Front. Zool.* **12**, 15 (2015).
152. Oulion, S., Bertrand, S. & Escriva, H. Evolution of the FGF gene family. *Int. J. Evol. Biol.* **2012**, 298147 (2012).
153. Setiamarga, D. H. et al. An in-silico genomic survey to annotate genes coding for early development-relevant signaling molecules in the pearl oyster, *Pinctada fucata*. *Zool. Sci.* **30**, 877–888 (2013).
154. Simakov, O. et al. Deeply conserved synteny resolves early events in vertebrate evolution. *Nat. Ecol. Evol.* **4**, 820–830 (2020).
155. Putnam, N. H. et al. Sea anemone genome reveals ancestral eumetazoan gene repertoire and genomic organization. *Science* **317**, 86–94 (2007).
156. Buenrostro, J. D., Giresi, P. G., Zaba, L. C., Chang, H. Y. & Greenleaf, W. J. Transposition of native chromatin for fast and sensitive epigenomic profiling of open chromatin, DNA-binding proteins and nucleosome position. *Nat. Methods* **10**, 1213–1218 (2013).
157. Zhang, Y. et al. Model-based analysis of ChIP-Seq (MACS). *Genome Biol.* **9**, R137 (2008).
158. Li, Q., Brown, J. B., Huang, H. & Bickel, P. J. Measuring reproducibility of high-throughput experiments. *Ann. Appl. Stat.* **5**, 1752–1779 (2011).
159. Heinz, S. et al. Simple combinations of lineage-determining transcription factors prime cis-regulatory elements required for macrophage and B cell identities. *Mol. Cell* **38**, 576–589 (2010).
160. Murata, M. et al. Detecting expressed genes using CAGE. *Methods Mol. Biol.* **1164**, 67–85 (2014).
161. Haberle, V., Forrest, A. R., Hayashizaki, Y., Carninci, P. & Lenhard, B. CAGEr: precise TSS data retrieval and high-resolution promoterome mining for integrative analyses. *Nucleic Acids Res.* **43**, e51 (2015).
162. Balwierz, P. J. et al. Methods for analyzing deep sequencing expression data: constructing the human and mouse promoterome with deepCAGE data. *Genome Biol.* **10**, R79 (2009).

Acknowledgements

We thank all members of the Hejnol laboratory for their continuous support, as well as the staff at the Norwegian Sequencing Centre and GeneCore (EMBL) for their technical support. We also thank R. Domínguez Acemel, M. Silva Magri and S. Jimenez Gancedo for their help with establishing ATAC-seq in *D. gyrociliatus*. We thank J. Tena-Aguilar for his help with ATAC-seq bioinformatic analyses and M. Ezcurra for providing live *C. elegans* worms for flow cytometry analyses. Finally, we thank A. de Mendoza and C. Laumer for a critical read of this manuscript, as well as M. Blaxter for comments and improvements. This study was supported by Sars Centre core budget and the European Research Council (ERC) grant agreement no. 648861 to A.H. J.M.M.-D. was additionally supported by the ERC grant agreement no. 801669, and B.C.V. by an EMBO Long-Term Fellowship (ALTF 74-2018). J.L.G.-S. received funding from the ERC (grant agreement no. 740041) and the Spanish Ministerio de Economía y Competitividad (grant no. BFU2016-74961-P) and the institutional grant Unidad de Excelencia María de Maeztu (MDM-2016-0687). We dedicate this manuscript to the loving memory of José Luis Gómez-Skarmeta.

Author contributions

J.M.M.-D., B.C.V., K.W. and A.H. conceived the study. J.M.M.-D., B.C.V. and A.H. designed experiments and analyses. J.M.M.-D. and V.C. performed collections and extractions. J.M.M.-D. and B.C.V. generated the genome and transcriptome assemblies. B.C.V. analysed the RNA-seq data. F.M. performed phylogenetic analyses and gene family evolution studies. V.C., A.K., N.B. and A.M.C.-B. performed gene expression analyses. W.G. performed flow cytometry analyses. N.C. and B.L. performed and analysed CAGE-seq. J.M.M.-D. and J.L.G.-S. performed and analysed ATAC-seq. J.M.M.-D., S.H., D.T., D.C., M.I., X.G.-B. and Y.M. performed computational analyses. All authors contributed to interpretation of the results. J.M.M.-D., K.W. and A.H. wrote the manuscript.

Competing interests

The authors declare no competing interests.

Additional information

Extended data is available for this paper at https://doi.org/10.1038/s41559-020-01327-6.

Supplementary information is available for this paper at https://doi.org/10.1038/s41559-020-01327-6.

Correspondence and requests for materials should be addressed to J.M.M.-D. or A.H.

Peer review information Peer reviewer reports are available.

Reprints and permissions information is available at www.nature.com/reprints.

Publisher's note Springer Nature remains neutral with regard to jurisdictional claims in published maps and institutional affiliations.

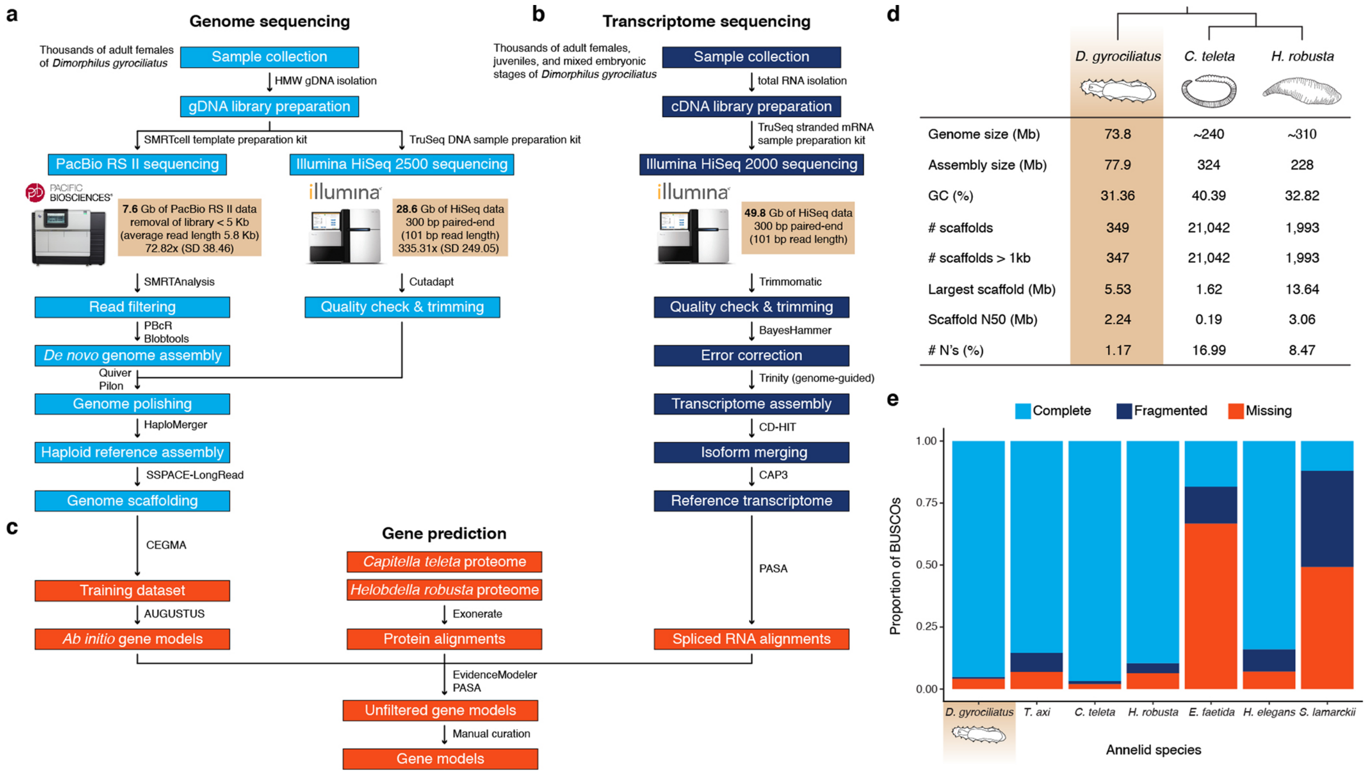

	D. gyrociliatus	*C. teleta*	*H. robusta*
Genome size (Mb)	73.8	~240	~310
Assembly size (Mb)	77.9	324	228
GC (%)	31.36	40.39	32.82
# scaffolds	349	21,042	1,993
# scaffolds > 1kb	347	21,042	1,993
Largest scaffold (Mb)	5.53	1.62	13.64
Scaffold N50 (Mb)	2.24	0.19	3.06
# N's (%)	1.17	16.99	8.47

Extended Data Fig. 1 | Sequencing approach and assembly statistics. a–c, Diagram of the approach taken to sequence and assemble *Dimorphilus gyrociliatus* genome and transcriptome, and to annotate coding genes in the genome. **d**, Comparison of genome assembly statistics between *D. gyrociliatus* and the annelids *C. teleta* and *H. robusta*. *D. gyrociliatus* genome is smaller than one third of *C. teleta*'s genome, and the assembly is contained in only ~350 scaffolds, with an N50 of 2.24 Mb, the second-best contiguity value for an annelid genome assembly to date. **e**, Genome completeness, as indicated by metazoan BUSCO repertoire, in genome assemblies of different annelid lineages. *D. gyrociliatus* completeness is comparable to *C. teleta*, the most conservative annelid genome sequence to date.

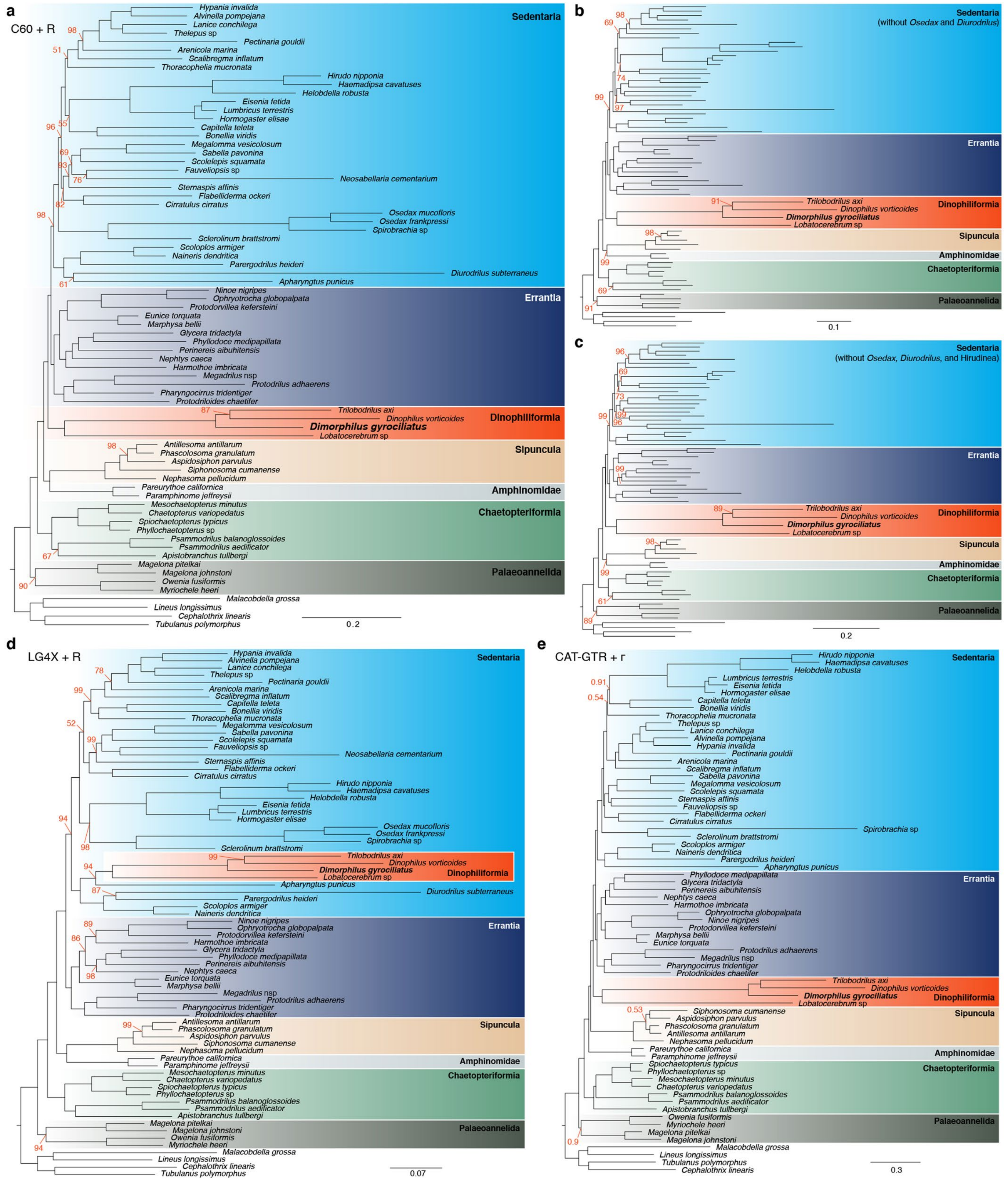

Extended Data Fig. 2 | *Dimorphilus gyrociliatus* phylogenetic position. a–c, Maximum likelihood phylogenetic tree using the site-heterogeneous model of protein evolution C60 + R and the entire annelid dataset (**a**), excluding the fast-evolving *Osedax* and *Diurodrilus* lineages (**b**), and additionally excluding Hirudinea (**c**). In all cases, *D. gyrociliatus* forms with *Trilobodrilus axi*, *Dinophilus vorticoides* and *Lobatocerebrum* sp. the clade Dinophiliformia, being this robustly placed as sister to Sedentaria + Errantia. **d**, Maximum likelihood tree using the site homogeneous model of protein evolution LG4X + R and the entire annelid dataset. This condition recapitulates Dinophiliformia, but places this group inside Sedentaria, related to other fast-evolving sedentarian lineages. **e**, Bayesian phylogenetic tree using the site-heterogeneous model of protein evolution CAT-GTR + Γ and excluding long branch lineages (*Osedax*, *Diurodrilus* and Hirudinea) recapitulates the maximum likelihood tree with the site heterogenous model and the same dataset. In all trees, only values other than 100 bootstrap or 1 posterior probability are shown.

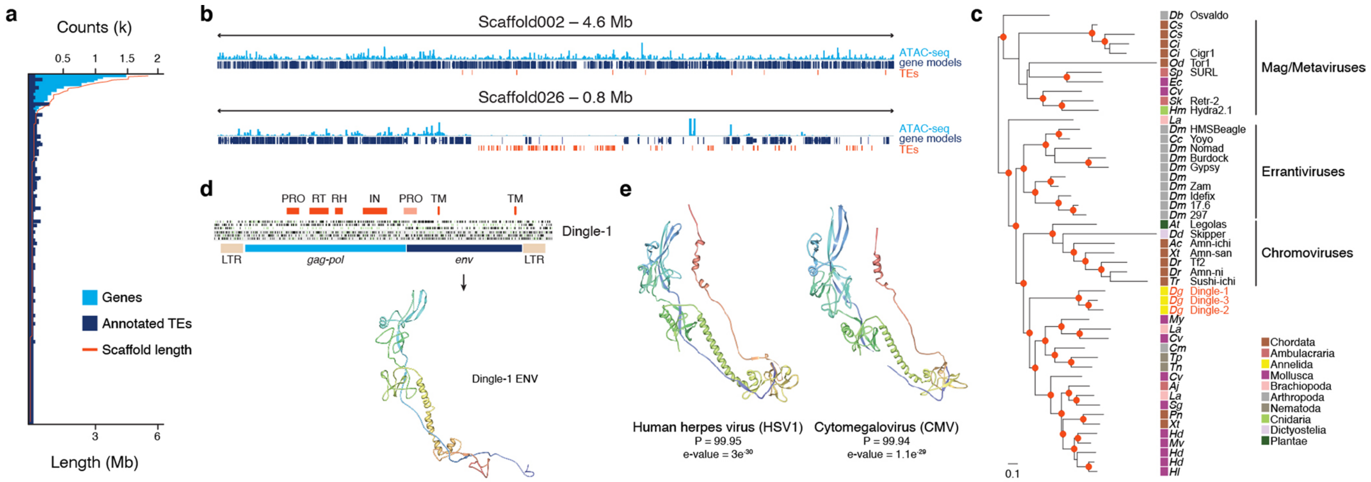

Extended Data Fig. 3 | The transposable element repertoire of *Dimorphilus gyrociliatus*. **a**, Graph showing the number of genes and transposable elements (TEs) per scaffold. **b**, Diagram of Scaffold002 and Scaffold026 illustrating how transposable elements (TEs, in red) often concentrate in gene-free (dark blue boxes) and closed chromatin (as indicated by ATAC-seq signal; light blue) islands. **c**, Maximum likelihood phylogeny of the *pol* gene showing that Dingle is a new family of *Ty3/gypsy* LTR element. The scale bar shows the number of substitutions per site and red dots are bootstrap values > 0.7. **d**, Genetic organization of Dingle, showing protein domains (top red boxes), 6-frame translations (green lines, ATG; black lines, stop codons) and the predicted protein structure of ENV, which shows resemblance to that of human herpes viruses **e**. In (**c**), Ac, *Anolis carolinensis*; Aj, *Apostichopus japonicus*; At, *Arabidopsis thaliana*; Cc, *Ceratitis capitata*; Ci, *Ciona intestinalis*; Cm, *Callosobruchus maculatus*; Cs, *Ciona savignyi*; Cv ; *Crassostrea virginica*; Db, *Drosophila buzzati*; Dd, *Dictyostelium discoideum*; Dg, *Dimorphilus gyrociliatus*; Dm, *Drosophila melanogaster*; Dr, *Danio rerio*; Ec, *Elliptio complanata*; Hd, *Haliotis discus hannai*; Hl, *Haliotis laevigata*; Hm, *Hydra magnipapillata*; La, *Lingula anatina*; Mv, *Mimachlamys varia*; My, *Mizuhopecten yessoensis*; Od, *Oikopleura dioica*; Pn, *Pundamilia nyererei*; Sg, *Saccostrea glomerata*; Sk, *Saccoglossus kowalevskii*; Sp, *Strongylocentrotus purpuratus*; Tn, *Trichinella nelson*; Tp, *Trichinella pseudospiralis*; Tr, *Takifugu rubripes*; Xt, *Xenopus tropicalis*.

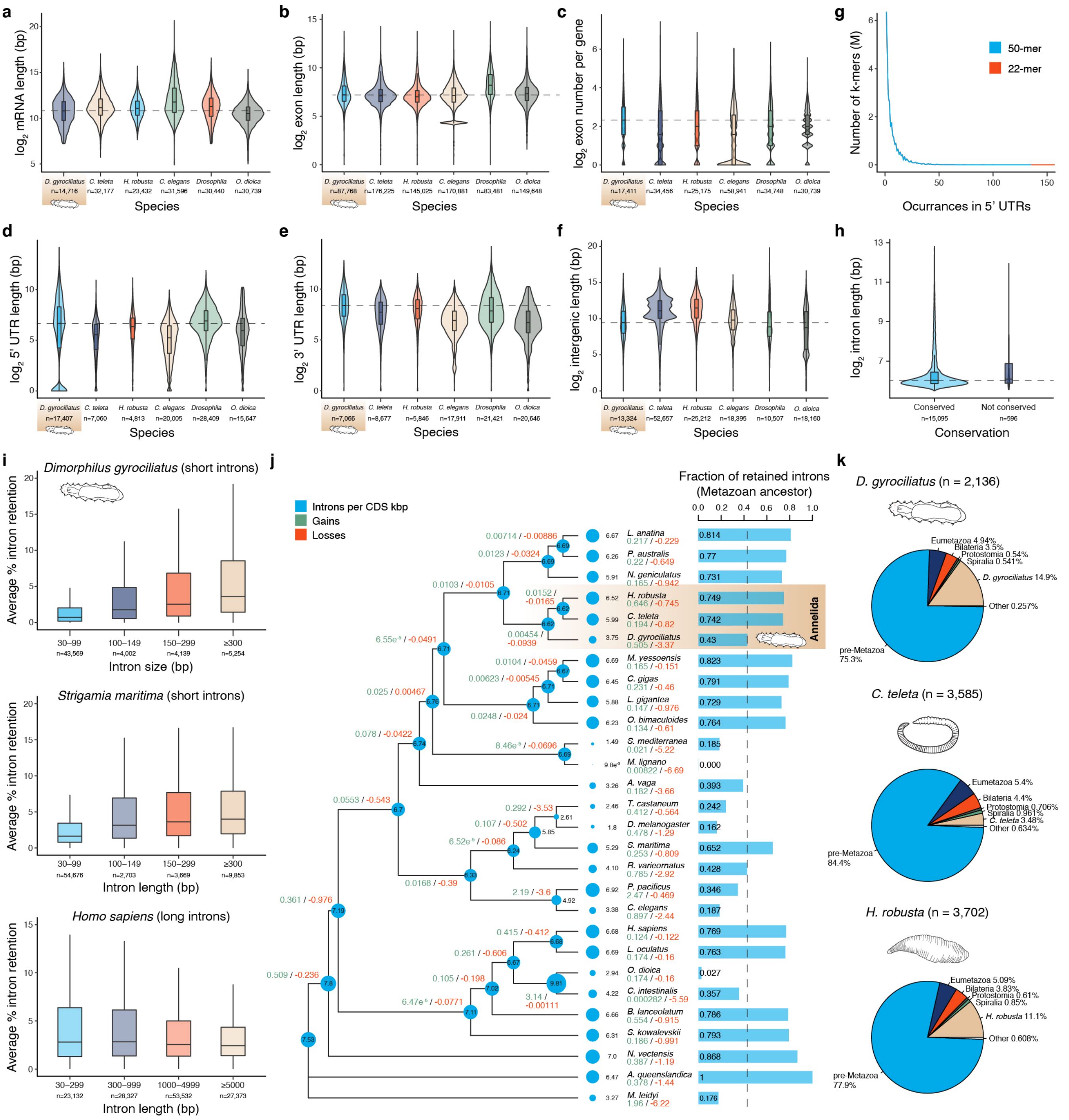

Extended Data Fig. 4 | Comparative analyses of gene structure features in the *Dimorphilus gyrociliatus* genome. a–f, Violin plots showing the genome-wide distribution of mRNA and exon lengths, exon numbers per gene, and the lengths of 5′ UTR, 3′ UTR and intergenic regions in *D. gyrociliatus*, the annelids *C. teleta* and *H. robusta*, and the bilaterians with compact genomes *C. elegans*, *D. melanogaster* and *O. dioica*. **g**, The distribution of occurrences of 22-mer and 50-mer in RNA-seq-based 5′ UTR regions of *D. gyrociliatus* does not indicate the presence of over-represented sequences that could act as splice leaders. **h**, Violin plot showing the distribution of intron sizes between conserved and non-conserved introns in *D. gyrociliatus*. **i**, The percentage of intron retention according to intron size demonstrates that the splicing machinery in *D. gyrociliatus* is adapted to short introns, as it occurs in the centipede *S. maritima* (also with short introns) and inversely to what is observed in *H. sapiens*, a species with longer introns. **j**, Metazoan-wide analysis of intron density, intron gain and intron loss rates per lineage and their ancestors. Intron density (blue circles) are indicated at each node and terminal tip of the phylogram. Net intron gains and losses are indicated below the species name, together with the fraction of introns conserved in each extant genome, among the ones inferred to have been present at the last metazoan common ancestor. *D. gyrociliatus* shows rates of intron loss and retention of ancestral introns similar to other animal lineages with much larger genomes. **k**, Inferred origin of the intron sites in *D. gyrociliatus* and the annelid *C. teleta* and *H. robusta*, expressed as the sum of gain probabilities at their respective ancestral nodes.

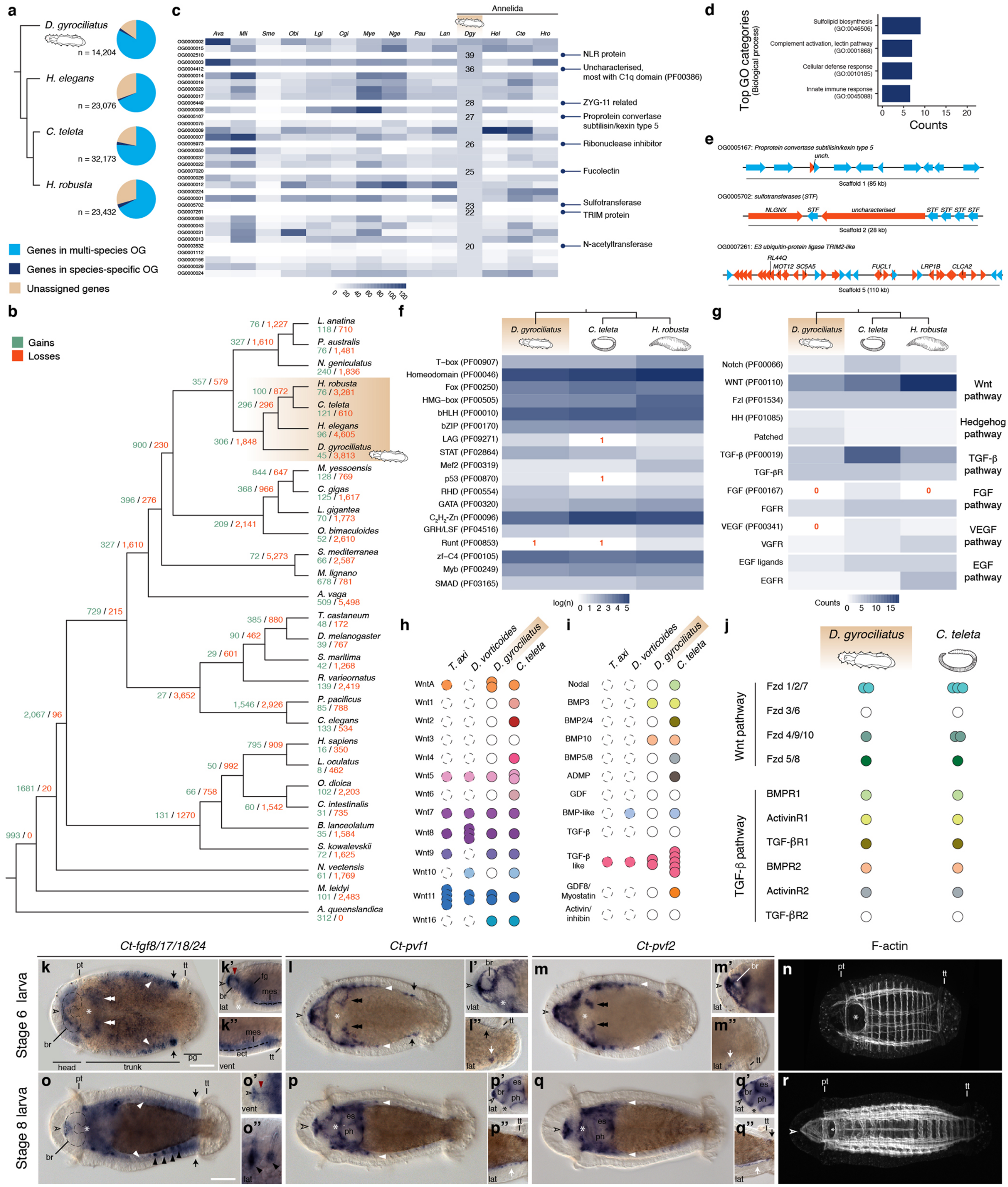

Extended Data Fig. 5 | See next page for caption.

Extended Data Fig. 5 | Expansions and gene losses in the genome of *Dimorphilus gyrociliatus*. **a**, Percentage of genes in multispecies orthogroups (OG; light blue) and species-specific orthogroups (dark blue and light brown) in the four studied annelid species. **b**, Metazoan-wide analysis of gene gain and loss, indicating the number of genes gained (in green) and lost (in red) at each node of the phylogram and the net value of gain/loss for each species. **c**, Heatmap of the 35 largest OG in *D. gyrociliatus*, indicating those that correspond to lineage-specific expansions (OG size indicated in the cell, and its putative orthology). **d**, Expanded families indicate that these are mostly involved in immunity and are mostly local copies (light blue, **e**). **f**, **g**, Heatmaps depicting the repertoire of transcription factors (TFs) and ligands and receptors in *D. gyrociliatus* and the annelids *C. teleta* and *H. robusta*. *D. gyrociliatus* lacks a clear ortholog of the FGF and VEGF ligand in *D. gyrociliatus*. Although *D. gyrociliatus* has retained all developmental signalling pathways, it has severely simplified the ligand repertoire of the Wnt signalling pathway (**h)**, and the TGF-β pathway (**i**), trend also observed in other members of Dinophilidae (dotted lines in *T. axi* and *D. vorticoides* indicate the reconstructed complements are based on transcriptomic data). **j**, However, *D. gyrociliatus* has a conserved repertoire of frizzled and TGF-β receptors. **k**–**m**, **o**–**q**, Differential interference contrast (DIC) micrographs of whole-mount *in situ* hybridization of *Capitella teleta* larvae of the FGF (*Ct-fgf8/17/18/24*) and VEGF (*Ct-pvf1* and *Ct-pvf2*) ligands and phalloidin staining at these points **n**, **r**. FGF and VEGF ligands are expressed in mesodermal derivatives anterior (open arrowhead) and dorsal to the brain (red closed arrowhead), associated with the foregut (double arrowheads), the longitudinal bands (white closed arrowheads), and the posterior growth zone (black and white arrows). FGF is also expressed in well-developed and nascent chaetoblasts (black closed arrowheads). br, brain; es, oesophagus; fg, foregut; lat, lateral; pg, pygidium; ph, pharynx; pt, prototroch; tt, telotroch; vent, ventral; vlat, ventrolateral. Scale bars, 50 µm. Asterisks mark the stomodeum.

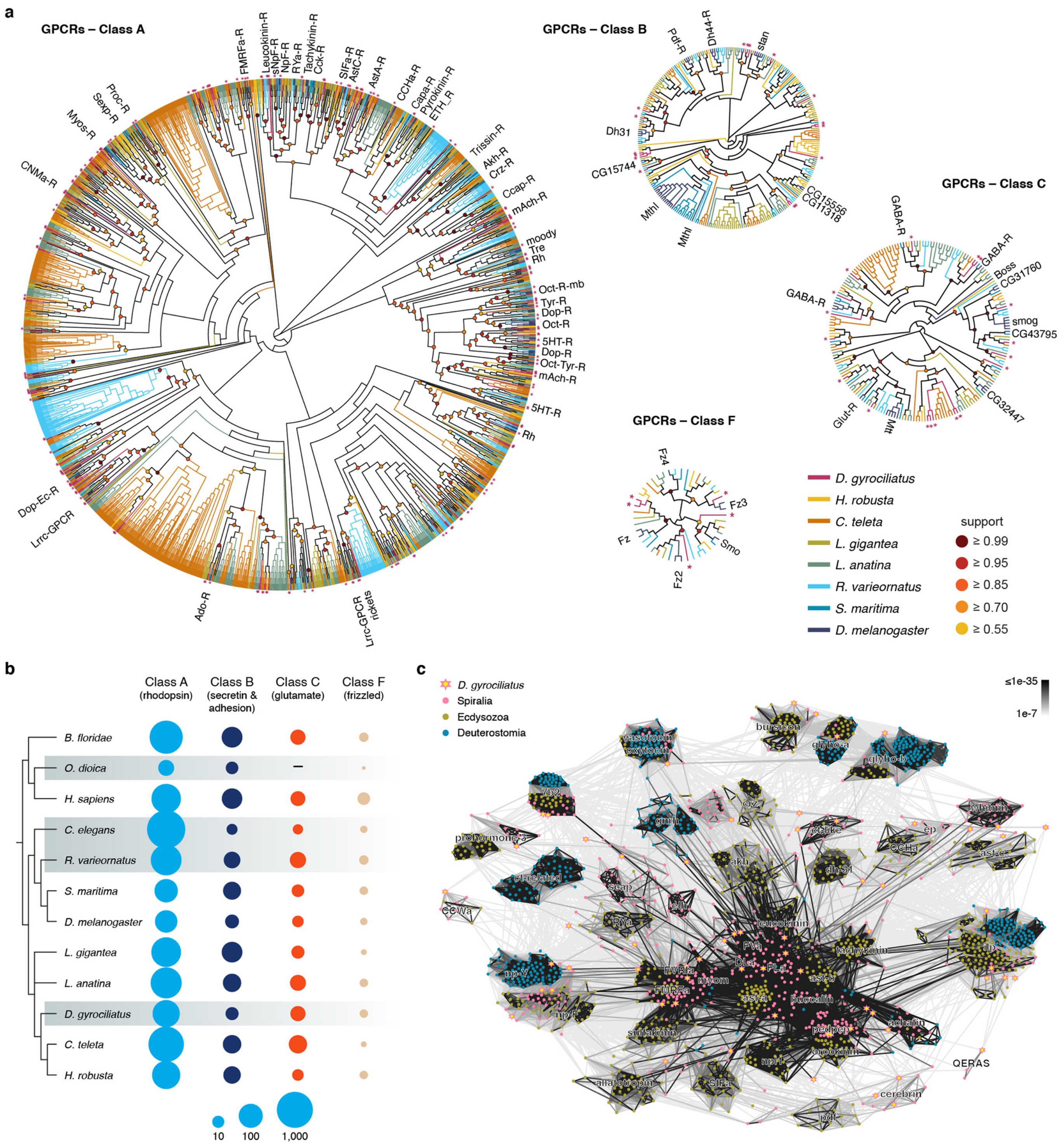

Extended Data Fig. 6 | See next page for caption.

Extended Data Fig. 6 | The GPCR and neuropeptide repertoire of *Dimorphilus gyrociliatus*. a, Orthology analyses of G-protein coupled receptors (GPCRs) for each class. The magenta asterisks highlight *D. gyrociliatus* receptors, and the annotations are given based on the *D. melanogaster* orthology. In (**a**) 5HT, serotonin; Ado, Adenosin; Akh, adipokinetic hormone; AstA, allatostatin A; AstC, allatostatin C; Boss, bride of sevenless; Capa, capability; Ccap, crustacean cardioactive peptide; CCHa, CCHamide; Cck, cholecystokinin; CNMa, CNMamide; Crz, corazonin; Dh, diuretic hormone; Dop, dopamine; Ec, ecdysteroid; ETH, ecdysis triggering hormone; FMRFa, FMRFamide; Fz, Frizzled; Glut, glutamate; Lrrc, leucine rich repeat containing; mAch, muscarinic acetylcholine; Mthl, methuselah; mtt, mangetout; Myos, myosuppressin; NpF, neuropeptide F; Oct, octopamine; Oct-R-mb, Octopamin receptor in mushroom bodies; Pdf, pigment dispersing factor; R, receptor; Rh, rhodopsin; RYa, RYamide; Sexp, sex peptide; SIFa, SIFamide; Smo, Smoothened; sNpF, short neuropeptide F; stan, starry night; Tre, trapped in endoderm; Tyr, tyramine. **b**, Phylogram with the number of GPCRs per class in representative animal species. Contrary to other animals with compact genomes and miniaturized morphologies, such as tardigrades, nematodes and appendicularians, *D. gyrociliatus* has a conserved GPCR repertoire. **c**, PSI-BLAST cluster map of *D. gyrociliatus* pro-neuropeptides, each dot corresponding to one sequence, their colour corresponds to the legend in upper left corner. Connections are based on *E* values < 1e-7 (see upper right corner). In (**c**), a, amide; ast, allatostatin; crz, corazonin; ct, calcitonin; dh, diuretic hormone; elh, ecdysis triggering hormone; ep, excitatory peptide; glyho-a, glycoprotein hormone alpha; glyho-b, glycoprotein hormone beta; gnrh, gonadotropin releasing hormone; ilp, insulin like peptide; myom, myomodulin; np-F, neuropeptide F; np-Y, neuropeptide Y; npl, neuropeptide-like; pdf, pigment dispersing factor; pedpep, pedal peptide; scap, short cardioactive peptide.

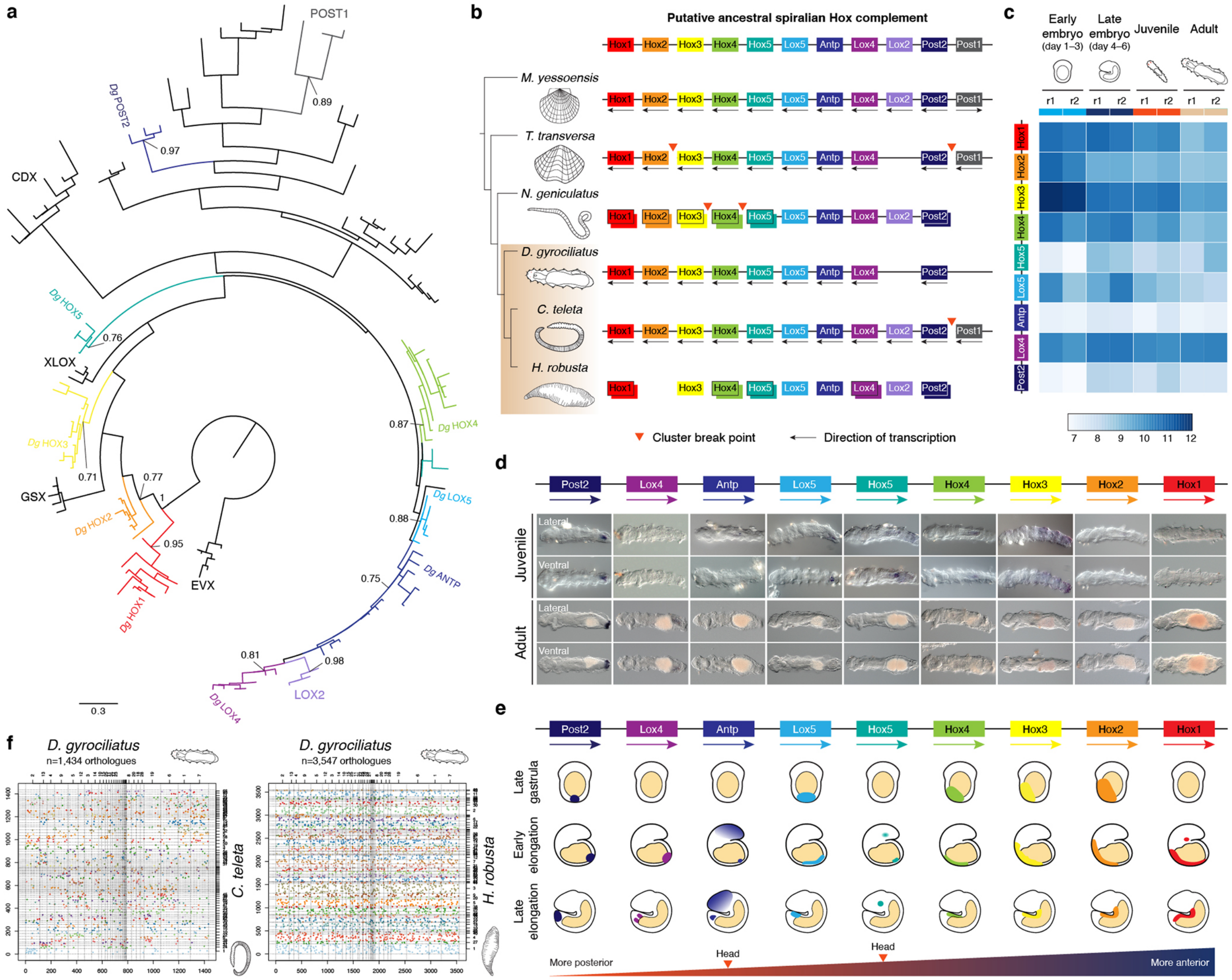

Extended Data Fig. 7 | The Hox cluster of *Dimorphilus gyrociliatus*. **a**, Maximum likelihood tree of Hox and ParaHox genes, with Evx proteins as outgroup, to assign orthology relationships of *Dimorphilus* Hox genes (indicated in the tree). Only bootstrap values for main orthogroups are shown. **b**, Schematic representation of Hox complements and Hox genomic organizations in representative spiralian species, with the putative ancestral spiralian Hox cluster on the top. Each Hox orthologous group is coloured differently. **c**, Heatmap of gene expression values of *Dimorphilus* Hox genes during the life cycle. **d**, Whole-mount in situ hybridization of Hox genes in *Dimorphilus* juveniles and adults. Only *Post2* and *Hox3* show conspicuous expression domains in the hindgut and posterior ectoderm of the juvenile, respectively. In adults, we only detect expression of *Post2* in the hindgut. **e**, Schematic summary of Hox gene expression in relation to the Hox genomic organization during *Dimorphilus* embryonic development. Hox genes exhibit an anteroposterior spatial collinearity along *Dimorphilus* trunk, with *Antp* and *Hox5* being additionally expressed in head domains. However, Hox genes do not exhibit temporal collinearity, as all but *Hox5*, *Antp*, and *Lox5* become expressed by the end of gastrulation. **f**, Oxford dot plots of orthologous genes between *D. gyrociliatus*, *C. teleta* and *H. robusta*. Macrosyntenic relationships are little conserved between annelid worms, indicating lineage-independent large-scale genomic reorganizations.

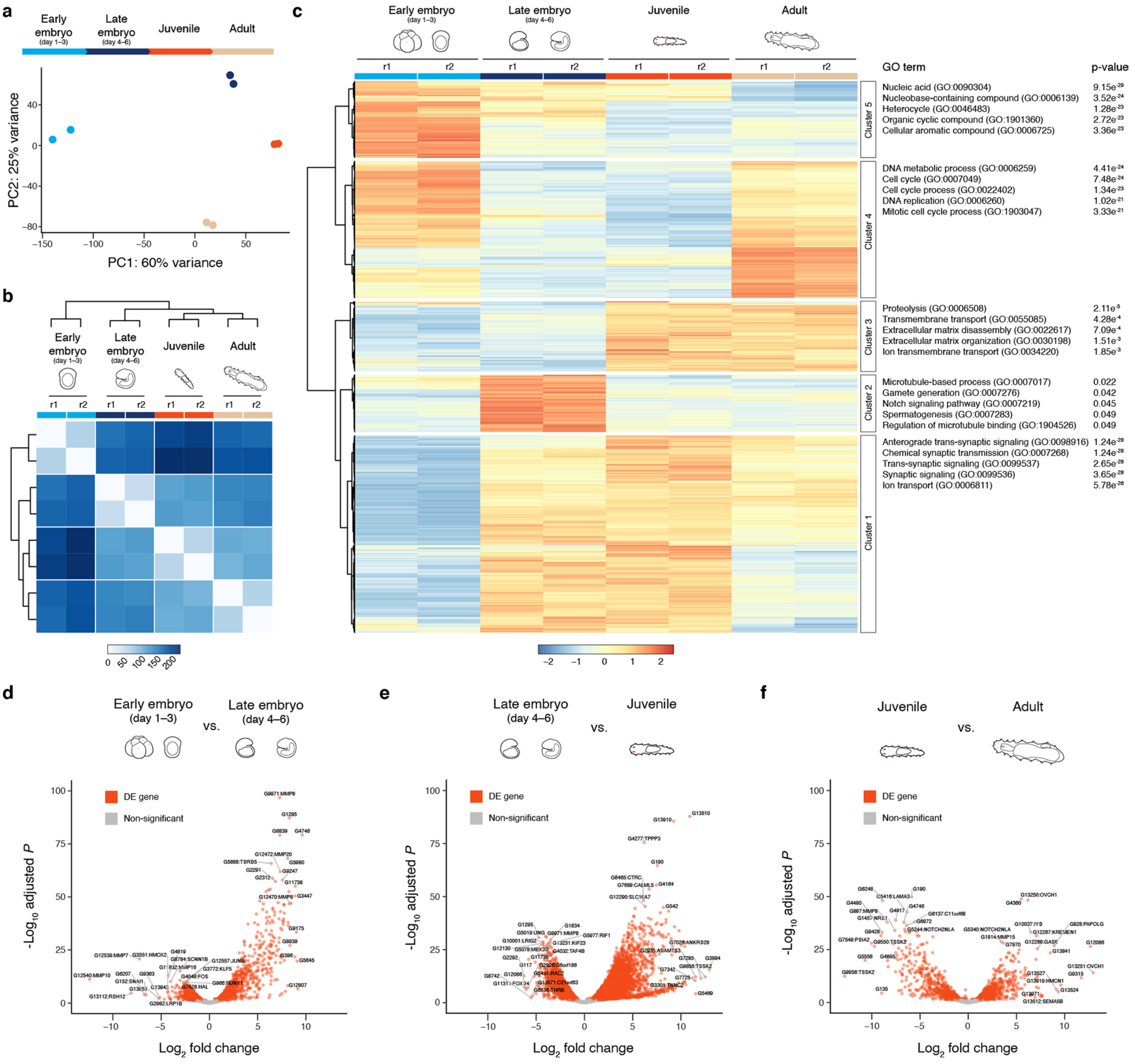

Extended Data Fig. 8 | Differential expression analyses during the life cycle of *Dimorphilus gyrociliatus*. **a**, Principal component analysis of the stage-specific RNA-seq samples using the top eight thousand most-variable genes. The raw count data was transformed to homogenize the variance and normalized using the variance-stabilizing method from DESeq2. **b**, Euclidean distances between the variance stabilized normalized counts of the stage-specific RNA-seq samples. **c**, Expression patterns for the top three thousand differentially expressed genes. Variance stabilized normalized counts were scaled around the mean value of the row to highlight changes in expression between developmental stages. Gene ontology terms associated with each cluster of expression profile are shown on the right. **d–f**, Differentially expressed genes from pairwise Wald tests between stage-specific RNA-seq samples. The top 18 genes with lowest p-adjusted values and highest log fold change are labelled. Considering gene expression changes significant if the adjusted p-value < 0.05, we identified 8,341 differentially expressed genes (4,543 up and 3,798 down) for 'late embryo vs early embryo'; 1,870 genes (938 up and 932 down) for 'juvenile vs late embryo'; and 3,746 genes (1,827 up and 1,919 down) for 'adult vs juvenile'.

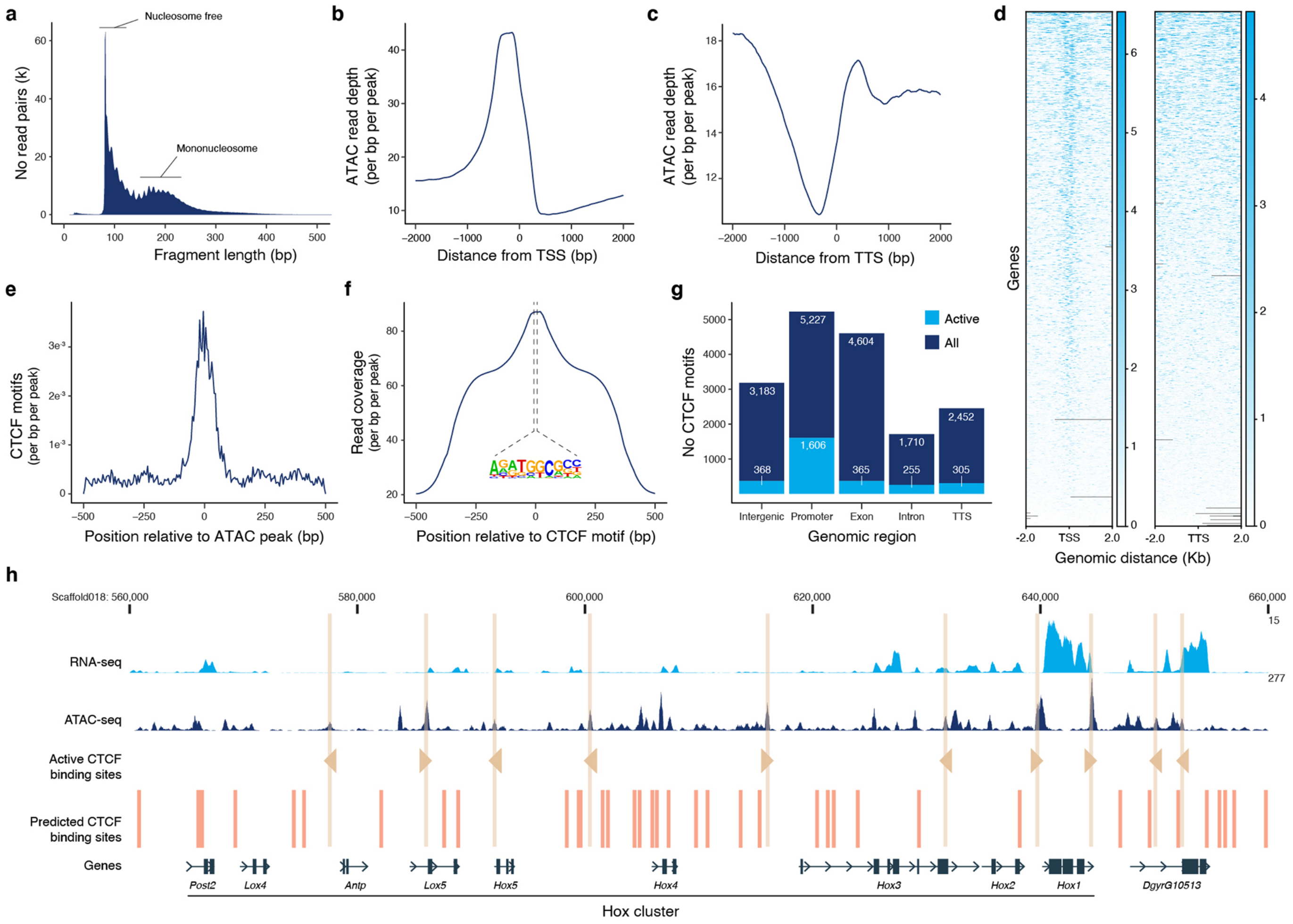

Extended Data Fig. 9 | CTCF-binding motifs are the most abundant in open chromatin regions in *Dimorphilus gyrociliatus*. a, Insert size distribution of ATAC-seq samples in *D. gyrociliatus*. **b**, **c**, Averaged ATAC-seq read depth around transcription start sites (TSS) and transcription termination sites (TTS). **d**, Heatmaps of ATAC-seq read coverage around TSS (left) and TTS (right) of each annotated gene. **e**, Averaged location of CTCF motifs in ATAC-seq peaks. **f**, Aggregate ATAC-seq read coverage centred around CTCF motifs. **g**, Number of CTCF motifs according to genomic feature. Most CTCF-binding motifs in open chromatin regions (that is 'active') are in promoters. **h**, Genome browser snapshot showing the distribution of CTCF-binding motifs in the Hox cluster of *D. gyrociliatus* as example of the general pattern observed genome wide. Most often, there is only one CTCF motif in an open chromatin region, and there is no clear directional arrangement between consecutive or neighbouring active CTCF-binding sites.

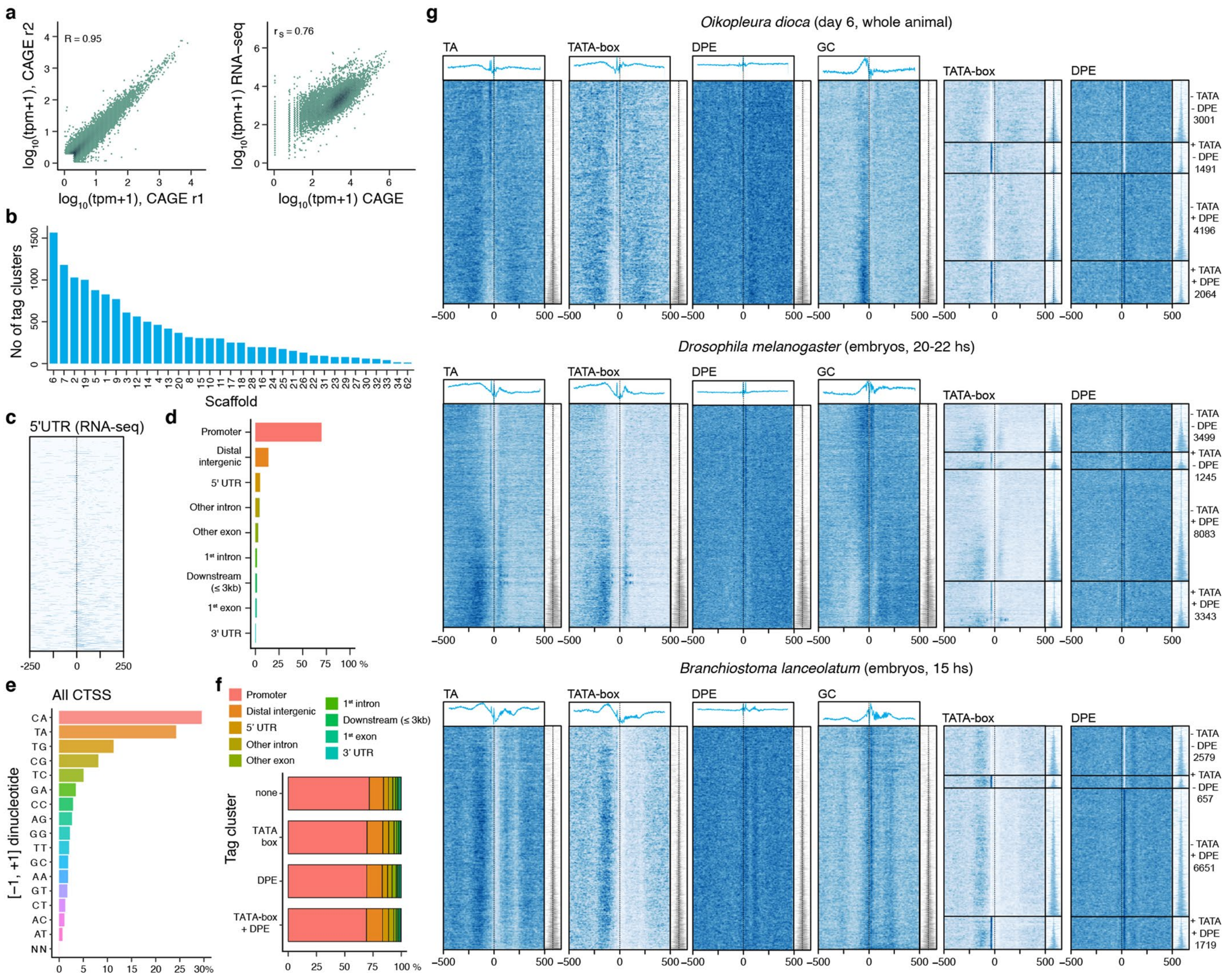

Extended Data Fig. 10 | General features and comparative aspects of CAGE-seq derived promoters in *Dimorphilus gyrociliatus*. **a**, Pearson's correlation at the CAGE-supported transcription start site (CTSS) level between CAGE-seq biological replicates (left panel) and Spearman correlation between gene-counts derived from RNA- or CAGE-seq (right panel, merged biological replicates). **b**, Distribution of number of tag clusters/promoters across scaffolds. **c**, Heatmap of tag-cluster coverage ordered by tag-cluster IQ-width from narrow (top) to broad (bottom) centred on the first nucleotide of 5′ UTRs determined by RNA-seq. **d**, Genomic locations of dominant CTSS. (**e**) Dinucleotide composition of all CTSSs identified in *Dimorphilus* CAGE-seq libraries. **f**, Genomic locations of tag clusters identified to contain a TATA-box or downstream promoter element (DPE). **g**, Sequence patterns in CAGE-seq derived promoters in the appendicularian *O. dioica* (genome size ~70 Mb), the fly *D. melanogaster* (genome size ~140 Mb) and the lancelet *B. lanceolatum* (genome size ~550 Mb). All heatmaps are centred on dominant TSSs and ordered by the tag-cluster/promoter IQ-width from narrower (top) to broader (bottom). IQ-widths are shown as tag-cluster coverage in the same order as on the heatmaps (right, in grey or blue). Heatmaps (left to right) represent TA dinucleotide patterns, TATA-box or DPE density (promoter regions are scanned using a minimum of the 80th percentile match to the TATA-box or DPE position weight matrix (PWM)) or GC dinucleotide patterns. Relative signal metaplot is shown above each heatmap. Promoters are divided according to TATA-box or DPE content at −30 or + 30 position relative to the dominant TSS, and a heatmap of TATA-box or DPE density across promoter categories is shown.

nature research

Corresponding author(s): Jose M Martin-Duran
Andreas Hejnol

Last updated by author(s): Apr 27, 2020

Reporting Summary

Nature Research wishes to improve the reproducibility of the work that we publish. This form provides structure for consistency and transparency in reporting. For further information on Nature Research policies, see Authors & Referees and the Editorial Policy Checklist.

Statistics

For all statistical analyses, confirm that the following items are present in the figure legend, table legend, main text, or Methods section.

n/a	Confirmed	
□	☒	The exact sample size (*n*) for each experimental group/condition, given as a discrete number and unit of measurement
□	☒	A statement on whether measurements were taken from distinct samples or whether the same sample was measured repeatedly
□	☒	The statistical test(s) used AND whether they are one- or two-sided *Only common tests should be described solely by name; describe more complex techniques in the Methods section.*
□	☒	A description of all covariates tested
□	☒	A description of any assumptions or corrections, such as tests of normality and adjustment for multiple comparisons
□	☒	A full description of the statistical parameters including central tendency (e.g. means) or other basic estimates (e.g. regression coefficient) AND variation (e.g. standard deviation) or associated estimates of uncertainty (e.g. confidence intervals)
□	☒	For null hypothesis testing, the test statistic (e.g. *F*, *t*, *r*) with confidence intervals, effect sizes, degrees of freedom and *P* value noted *Give P values as exact values whenever suitable.*
□	☒	For Bayesian analysis, information on the choice of priors and Markov chain Monte Carlo settings
☒	□	For hierarchical and complex designs, identification of the appropriate level for tests and full reporting of outcomes
□	☒	Estimates of effect sizes (e.g. Cohen's *d*, Pearson's *r*), indicating how they were calculated

Our web collection on statistics for biologists contains articles on many of the points above.

Software and code

Policy information about availability of computer code

Data collection	No software was used to collect data for this study
Data analysis	We used the following open source software in this study: SMRTAnalysis (v.2.3.0.140936), PBcR (v.8.3rc2), Blobtools (v.0.9.16), Pilon (v.1.16), cutadapt (v.1.4.2), HaploMerger2 (v.20151124), SSPACE-LongRead (v.1.1), trimmomatic (v.0.35), SPAdes (v.3.6.2), Super_Deduper (v.2.0), Platanus (v.1.2.4), Quast (v.3.1), BWA-MEM (v.0.7.12-r1044), SAMtools (v.1.3.1), BUSCO (v2), BLAT (v.36x2), Isoblat (v.0.3), Picard tools (v.2.0.1), Jellyfish (v.2.2.3), Trinity (v2.1.1), Bowtie2 (v.2.1.0), CD-HIT (v.4.6), CAP3 (v.02/10/15), Kallisto (v0.44.0), DESeq2, Transdecoder (v5.0.2), HMMER (v.2.3.2), MSAProbs (v0.9.7), BGME, IQTREE, RepeatModeler (v.1.0.4), MITE Digger, MODELLER, CEGMA (v.2.4), AUGUSTUS (v.3.2.1), EXONERATE (v.2.2.0), PASA (v.2.0.2), GMAP (v.2015-12-31), EvidenceModeler (v.1.1.1), ORFik, BLAST (v.2.2.31+), Trinotate (v.3.0), signalP (v.4.1), tmHMM (v.2.0c), MAFFT (v7.310), Malin, OrthoFinder (v.2.2.7), FastTree (v.2), Clustal X, trimAl, MacVector (v.11.0.4), Adobe Photoshop CS6, Adobe Photoshop CC (v.14.0), Adobe Illustrator CC (v.17.0.0), MACS2 (v.2.1.1.20160309), IDRCode, HOMER (v2), CAGEr (v.1.20.0), KAT, GenomeScope2.0, BBTools

For manuscripts utilizing custom algorithms or software that are central to the research but not yet described in published literature, software must be made available to editors/reviewers. We strongly encourage code deposition in a community repository (e.g. GitHub). See the Nature Research guidelines for submitting code & software for further information.

Data

Policy information about availability of data

All manuscripts must include a data availability statement. This statement should provide the following information, where applicable:

- Accession codes, unique identifiers, or web links for publicly available datasets
- A list of figures that have associated raw data
- A description of any restrictions on data availability

All new raw sequence data associated to this project are available under project with primary accession PRJEB37657 in the European Nucleotide Archive (ENA). Genome annotation files and additional datasets are available in https://github.com/ChemaMD/DimorphilusGenome.

Field-specific reporting

Please select the one below that is the best fit for your research. If you are not sure, read the appropriate sections before making your selection.

☒ Life sciences ☐ Behavioural & social sciences ☐ Ecological, evolutionary & environmental sciences

For a reference copy of the document with all sections, see nature.com/documents/nr-reporting-summary-flat.pdf

Life sciences study design

All studies must disclose on these points even when the disclosure is negative.

Sample size	Sample sizes for genomic, transcriptomic and CAGE-seq analyses were estimated based on the amount of genomic DNA and total RNA obtained per individual. For ATAC-seq analyses, sample size was estimated in order to obtain a final number of 50,000 nuclei for subsequent tagmentation.
Data exclusions	No data was excluded from the analyses.
Replication	All RNA-seq, ATAC-seq and CAGE-seq analyses were conducted in replicates.
Randomization	All animal collections were performed randomly.
Blinding	All animal collections were allocated blindly to any of the replicates of study.

Reporting for specific materials, systems and methods

We require information from authors about some types of materials, experimental systems and methods used in many studies. Here, indicate whether each material, system or method listed is relevant to your study. If you are not sure if a list item applies to your research, read the appropriate section before selecting a response.

Materials & experimental systems

n/a	Involved in the study	
☒	☐	Antibodies
☒	☐	Eukaryotic cell lines
☒	☐	Palaeontology
☐	☒	Animals and other organisms
☒	☐	Human research participants
☒	☐	Clinical data

Methods

n/a	Involved in the study	
☒	☐	ChIP-seq
☐	☒	Flow cytometry
☒	☐	MRI-based neuroimaging

Animals and other organisms

Policy information about studies involving animals; ARRIVE guidelines recommended for reporting animal research

Laboratory animals	This manuscript uses the laboratory strains of the annelid species Dimorphilus gyrociliatus and Capitella teleta. For D. gyrociliatus, we used adult females and stage-specific embryonic samples. For C. teleta, we studied larval stages.
Wild animals	This study does not involve wild animals.
Field-collected samples	This manuscript studies the annelid species Trilobodrilus axi, which was collected from the wild by the lab of Katrine Worsaae. Adult specimens were kept in filtered seawater (31 ppm) at 15 ºC in the dark prior collection for genomic DNA extraction.
Ethics oversight	Work on annelid embryos are not subject of ethical approvals or restrictions.

Note that full information on the approval of the study protocol must also be provided in the manuscript.

Flow Cytometry

Plots

Confirm that:

☒ The axis labels state the marker and fluorochrome used (e.g. CD4-FITC).

☒ The axis scales are clearly visible. Include numbers along axes only for bottom left plot of group (a 'group' is an analysis of identical markers).

☒ All plots are contour plots with outliers or pseudocolor plots.

☒ A numerical value for number of cells or percentage (with statistics) is provided.

Methodology

Sample preparation	Hundreds of adult females of D. gyrociliatus were collected and starved for 3–4 days before flow cytometry analysis. Worms were transferred into a petri dish, washed well in seawater to remove any contaminant, and finely chopped with a razor blade in 2 ml of General-Purpose Buffer to generate a suspension of nuclei. This suspension was filtered through a 30 µm nylon mesh and stained with propidium iodide (Sigma; 1 mg/mL) on ice.
Instrument	We used a flow cytometer Partec CyFlow Space fitted with a Cobalt Samba green laser (532nm, 100mW)
Software	We used the built-in instrument software FloMax
Cell population abundance	We used flow cytometry to estimate genome size using C. elegans as reference and thus we did not sort any cell populations. To estimate genome size from propidium iodide staining, we did three independent runs for each species analysing at least 1,000 nuclei per run.
Gating strategy	We considered all cell populations for genome size estimation, and thus no gating strategy was implemented.

☒ Tick this box to confirm that a figure exemplifying the gating strategy is provided in the Supplementary Information.